F. Piscaglia, A. Onorati, S. Marelli, M. Capobianco
A Detailed One-Dimensional Model to Predict the Unsteady Behavior of Turbocharger Turbines for Internal Combustion Engine Applications
International Journal of Engine Research, Vol. 20, N. 3, 2019, p. 327-349
doi:10.1177/1468087417752525

A detailed 1D model to predict the unsteady behavior of turbocharger turbines for IC engines applications

F. Piscaglia[1], A. Onorati[1], S. Marelli[2] and M. Capobianco[2]*
[1] Dipartimento di Energia, Politecnico di Milano, Italy
[2] DIME, University of Genoa, Genoa, Italy

Abstract
This paper describes an investigation of the unsteady behaviour of turbocharger turbines by 1D modeling and experimental analysis. A one-dimensional model has been developed to predict the performance of a vaneless radial-inflow turbine submitted to unsteady flow conditions. Differently from other approaches proposed in the literature, the turbine has been simulated by separating the effects of casing and rotor on the unsteady flow and by modeling the multiple rotor entries from the volute. This is a simple and effective way to represent the turbine volute by a network of 1D pipes, in order to capture the mass storage effect due to the system volume, as well as the circumferential variation of fluid dynamic conditions along the volute, responsible for variable admittance of mass into the rotor through blade passages.
The method developed is described and the accuracy of the 1D model is shown by comparing predicted results with measured data, achieved on a test rig dedicated to the investigation of automotive turbochargers. The validation of the code is presented and an analysis of the flow unsteadiness, based on a variety of parameters, is proposed.

Keywords
Unsteady behavior of turbocharger turbine, IC engine simulation, experimental analysis, 1D unsteady flows, turbine modeling.

Date received: XXX; reviewed: XXX; accepted: XXX

Nomenclature

Acronyms

BSR	blade speed ratio
GDI	gasoline direct injection
ICE	internal combustion engine
MFP	turbine mass flow parameter
MOC	method of characteristics
MR	normalized mass flow ratio
PR	pressure ratio
PRBC	partially reflecting boundary condition
RPM	rotational speed
VGT	variable geometry turbine
VVA	variable valve actuation

Definitions

A_A	non-dimensional entropy level
a_A	entropy level
aSt	acoustic normalized Strouhal number
c_{is}	isentropic expansion velocity
c_p	specific heat at constant pressure

* Corresponding author. Tel.: +39-010-3532443; fax: +39-010-3532566
Email address: silvia.marelli@unige.it

f_w wall friction coefficent
k specific heat ratio
$\dot{m}_{ratio}$ normalized mass flow ratio
N_S turbine rotational speed parameter
n_c number of cycles per second
$pmSt$ pressure wave normalized" Strouhal number
R gas constant
St Strouhal number
$\bar{W}$ cycle-average turbine power

Greeks
β reduced frequency
η_{TS} turbine isentropic total-to-static efficiency
λ^* Starred Riemann variable

Notation

A non-dimensional speed of sound
a speed of sound
e internal energy
D diameter
d turbine diameter
Err error
F pipe area
f pulse frequency
G turbine mass flow rate factor
M mach number
$\dot{m}_{ratio}$ mass flow rate
n rotational speed
p pressure
q rate of heat transfer per unit mass
T temperature
U non-dimensional particle velocity
u flow velocity

Greeks
β reduced frequency
ε turbine pressure ratio
η efficiency
λ Riemann variable
λ_{in} incident Riemann variable
λ_{out} reflected Riemann variable
ρ density
Φ pulse length as a fraction of wavelength (duty cycle)
ω angular frequency

Subscripts
B,C measurement point in Fig.(4)
$conv$ convergent duct
exp experimentally measured

fit fitting procedure
i instantaneous
max maximum
mean average value
norm normalized
opt optimum
ref reference condition
real real condition
rot rotor
S isentropic condition
sim simulated
0 total condition
1 turbine inlet
2 turbine outlet

1 Introduction

The reduction of fuel consumption and exhaust emissions is today a fundamental target for automotive engines, due to the increasing cost of fuels and the need to control CO_2 emissions [1]. This requirement is more significant for Spark Ignition engines, especially at part load operation, whilst maintaining current specific power levels, low exhaust emissions and an excellent vehicle driveability. To achieve this target, the full integration of different technologies such as downsizing, turbocharging, Gasoline Direct Injection (GDI), Variable Valve Actuation (VVA) and after-treatment systems, must be accomplished [2]-[4]. As regards turbocharging, the optimization of turbochargers is an essential step, requiring a better knowledge of turbine and compressor performance over an extended range. The availability of experimental information on turbocharger behaviour can help to enhance numerical simulation models, extremely useful to guide the choice of the turbocharging system for a specific engine. In this field, one-dimensional (1D) models are currently used successfully to perform engine-turbocharger matching calculation. Generally, a quasi-steady approach is followed, on the basis of compressor and turbine characteristic maps [5], which usually require the adoption of mathematical techniques for the extrapolation. Moreover, the real compressor and turbine behaviour differs from the steady flow characteristic maps, due to unsteadiness of the flow caused

by the opening and closing of intake and exhaust valves, more evident in downsized engines [6]-[9].

With special reference to turbocharger turbines, it is well known that the typical flow through the turbomachine never reaches the steady conditions under which its performance was measured. Plots of efficiency against mass flow parameter show that instantaneous values deviate substantially from the steady state curve [10]-[12]. Since the turbine often works under off-design and unsteady flow conditions, the estimation of its performance at such conditions is as important as that at the design point. In particular, under unsteady flow conditions, the expansion ratio and the turbine power are usually underestimated, while the mass flow is over-predicted. The experimental work at Purdue University [13] has suggested that the IC engine flow arriving at the turbine inlet is comprised of both convective and inertial flow with pressure propagation (wave action) effects. In 1D simulation, traditional quasi-steady turbine models assume that the unsteady performances can be predicted by a straightforward interpolation of the steady flow mass and efficiency characteristics, but there are some limits. First, a quasi-steady approach is satisfactory only for devices having relatively small lengths and volumes: its application to a radial-flow turbocharger is not completely acceptable, due to the significant volume of the turbine volute, especially if the nature of the incoming flow is pulsating. Besides, turbocharger performance under unsteady flow differs from that produced under cycle averaged conditions and deviates much more at lower engine rotational speed levels, with the waste-gate valve open.

The aim of this work is to improve the 1D modeling tools for IC engine turbochargers, investigating the flow conditions in a turbine under pulsating flow conditions and exploring the mechanisms to enhance energy transfer. This research starts from previous work carried out by Chen and Winterbone [14], by Chiong et al. [15], by Serrano et al.

[12], [16] and by the authors of this paper [17]. In [12], [14]-[16], a tapered pipe was used to represent the volute; the pipe finished with an open end, or rather, the entire flow was forced to pass through the rotor in one go, at the same point. In [17] the authors proposed to model the volute and the diffuser by a 0-D volume, to consider the effect of the flow storage under unsteady operating conditions, and by a duct, whose length should account for the wave propagation time from a nominal entry and the rotor itself. A boundary condition based on the steady state maps was employed to model the turbine rotor and predict the expansion ratio. The simulation results showed a strong dependence on the pulsations along the pipes downstream of the turbine. Despite predictions of the hysteresis loop could still not be considered satisfactory, it was found that the main issues to solve, in order to correctly capture the unsteady flow phenomena, were the correct prediction of the wave motion downstream of the turbine, together with a correct definition of the effective position of the turbine boundary, halfway around the casing. The apparent length required to calculate the time lag was defined by assuming the rotor entry position at 180° from the volute tongue, according to the approach adopted by other researchers [11]. The limits shown in [17] inspired the enhancements presented in this work. First, the classical Lax-Wendroff numerical scheme for the solution of the governing equations in the inner nodes was replaced by a staggered second order explicit solver [18], in order to preserve sharp value changes in the pressure and velocity fields across the turbine rotor and achieve a high accuracy of mass conservation. Then, different approaches to model the turbocharger have been proposed and tested by the in-house 1D numerical code GASDYN, developed by the authors; finally, simulation results have been compared with the experimental data carried out at the University of Genoa. In order to model the experimental test rig, “ad-hoc” boundary conditions have been developed to simulate an inlet rotating valve and a partially reflecting outlet end (PRBC) [19]. As will be discussed,

simulations and experimental measurements presented in this work were carried out with cold flow, in order to neglect the effects of the heat transfer.

Experimental investigations were conducted at the turbocharger test rig of the University of Genoa [10], [20], shown in Figure l. An air supply system, characterized by three electrical screw compressors, is able to provide a total mass flow rate up to 0.6 kg/s at a pressure of 8 bar. An electrical heater is used to increase air temperature up to 1000 K, to prevent water from condensing and freezing at the turbine outlet. The turbocharger rotational speed is controlled by a compressor, which acts as a dynamometer. In particular, compressor's power absorption is controlled by regulating the pressure level at the compressor inlet. In the test-rig used for experimental measurements, two pulse generator systems can be used to reproduce unsteady flow conditions occurring in a turbocharged reciprocating engine. The former is based on rotating valves with a diametral slot driven by a variable speed motor, the latter is fitted with a motor driven engine head, which generates a controlled pulsating flow upstream of the turbine or downstream of the compressor. Results reported in this paper refer to an unsteady flow generated by the rotating valve device. This system allows to control the main pulsating flow characteristics (mean value, amplitude, shape and frequency of pressure oscillations) at the turbine inlet. The experimental investigations were performed on a small automotive turbocharger (IHI RI-IF3) matched to a SI engine. A single entry nozzleless radial flow turbine (maximum impeller diameter equal to 33 mm) was fitted with a waste-gate valve. Measurements under unsteady flow conditions were performed by an automatic data acquisition system, using interactive procedures in LabVIEW® environment. Instantaneous parameters were measured at different locations along the circuit, upstream and downstream of the turbine (Figure l). Static inlet and outlet pressure, mass flow rate and turbocharger rotational speed were instantaneously measured through

two high-speed synchronized data acquisition cards. To start data acquisition on both cards, a trigger signal corresponding to a definite position of the rotating valve was sent to the master card. Pressure signals were measured through high frequency response strain gauge sensors, characterized by an accuracy of ±0.15% of the full scale. Each transducer was mounted near the duct wall, to avoid signal distortion related to the connecting line. The sampling rate was selected to draw pressure profiles with about 150 points over a complete cycle.

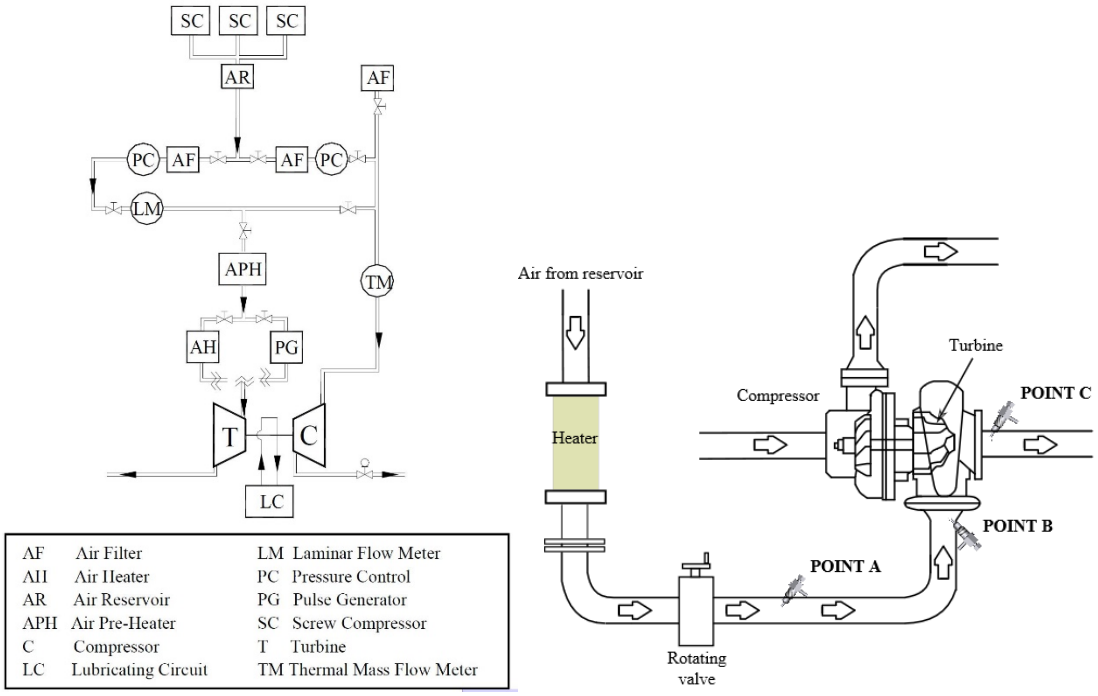

Figure 1. *Schematic layout of the experimental test rig at the University of Genoa (left-hand side) and measuring stations employed (right-hand side).*

Platinum resistance thermometers were adopted to record the mean temperature levels with an uncertainty of ± 0.15 °C + 0.2% of measured value. Since temperature fluctuations under unsteady flow conditions should be considered, in order to correct the output voltage of the hot wire probe used to measure mass flow rate, the instantaneous levels were evaluated referring to an adiabatic process of an ideal gas, starting from

measured mean inlet static pressure (indicated as p_{1mean} in Eq.1) and temperature (T_{1mean} in Eq.1) and instant static pressure (p_{1i} in Eq.1), as follows:

$$T_{1i} = T_{1mean} \cdot \left(\frac{p_{1i}}{p_{1mean}}\right)^{\frac{k-1}{k}} \quad (1)$$

This simplified method allows to accurately describe temperature fluctuations in the case of cold air tests, as shown in Figure 2.

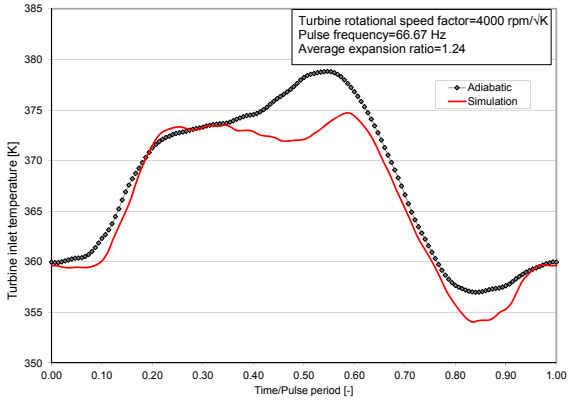

Figure 2. *Comparison between simulated and calculated (adiabatic process) temperature profiles.*

A good agreement was found with measured values in [11] and with the results provided by 1D simulation models in [17]. The average turbine mass flow rate was measured through a laminar flow meter, while the instantaneous level at the turbine inlet was detected using a hot-wire anemometric system. Under pulsating flow conditions, the sample rate was adjusted in order to describe mass flow rate traces containing about 150 points in a complete cycle; to eliminate high frequency disturbances, a central moving average filtering technique was adopted. The filtered signals were then processed to calculate the average diagram over a large number (about 50 consecutive cycles). The fibre film probe was calibrated against a laminar flow meter for three different air temperature levels, selected to include unsteady instantaneous conditions. The output probe voltage was then corrected according to the temperature variation during the pulse

cycle. The uncertainty in mass flow measurement was about ±2 per cent throughout the calibration range. The turbocharger rotational speed measurement was performed through an eddy current probe mounted close to the compressor wheel. This system is characterized by a full-scale frequency precision of ±0.009 per cent, besides it allows to detect rotor blades passage for each revolution with good accuracy. For each operating condition (pulse frequency and mean expansion ratio), measurements were conducted at a constant turbine rotational speed parameter. Turbine maps were measured by changing the compressor power absorption. All the signals reported in the paper are an ensemble average of several consecutive cycles. In the present work, measurements were performed at a rotational speed parameter of about 4000 rpm/√K, with the waste-gate valve fully closed. Even if the rotational speed fluctuations during the pulse cycle are small, an accurate evaluation of instantaneous rotational speed makes it possible to assess the turbocharger angular acceleration, and therefore the fluctuating component of actual turbine power used to assess instantaneous efficiency [21]. As an example of this aspect, in Figure 3 the instantaneous parameters concurring in the definition of turbine efficiency are shown; all signals were phase shifted by considering that the pulse travels at the local sonic velocity added to the local flow velocity, accordingly to [11]. Therefore, the torque signal was shifted forward in time relative to mass flow and pressure, to achieve the proper conditions [21].

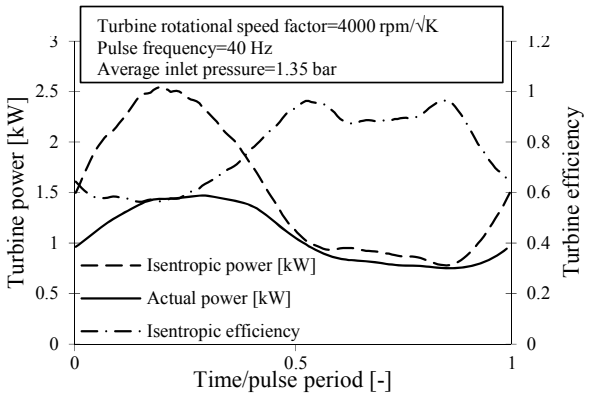

Figure 3. *Instantaneous turbine performance – experimental results.*

2 Turbine model development

The experimental test rig reported in Figure l has been modeled by the one dimensional code GASDYN [22], developed by the authors. The domain modeled included the part of the test bench between the rotating valve and the physical outlet end of the system (ambient), as shown in Figure 4.

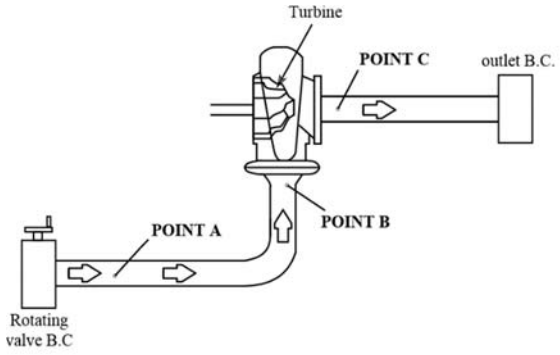

Figure 4. *Modeled part of the experimental test bench, starting from the rotating valve and ending at the physical outlet (in ambient).*

In order to accomplish this task, an "ad-hoc" development of the one-dimensional code was required to model:

- the rotating valve [17];

- the unsteady behavior due to the turbine casing;

- the reflection of acoustic waves at the outlet end [19], to improve the accuracy of the predicted wave motion downstream of the turbine (see Appendix B);

Additionally, algorithms to extrapolate turbine performance and efficiency data maps supplied by the manufacturer were needed, to favour the code convergence (see Appendix A).

The solution of governing equations of the boundary conditions implemented in this work is based on the Method of Characteristics (MOC), which provides a natural mechanism for propagating the information required by the boundary calculation across the pipe end meshes. A staggered second order explicit solver has been used in the internal domain for

an accurate solution of the unsteady flow governing equations, even when sharp value changes in pressure and velocity fields are present, as typically occurs near the turbine.

To reproduce the experimental conditions, flow temperature at the inlet was set to 400 K in the simulations; hence, the heat transfer at the duct walls was negligible. The mean expansion ratio across the turbine ε_{mean} was set by regulating the mean inlet pressure, whereas the turbine rotational speed parameter $n/\sqrt{T_{01}}$ (where n is the turbocharger rotational speed and T_{01} is the total temperature at the inlet section) was set to 4000 rpm/√K. Three pulse frequencies were tested (40 Hz, 70 Hz, 100 Hz), corresponding to the dominant excitation of a four-cylinder, four-stroke engine at 1200, 2000, 3500 rpm.

In the majority of models developed for vaned turbines, the effect of the turbine casing is usually neglected [23]; by contrast, it plays an important role in specifying the inlet condition for the rotor, hence it must be considered to achieve an accurate simulation approach. In the proposed model, the flow in the turbine casing is assumed to be divided into two stages: in the first stage, the fluid flows from the turbine entry to the tip of the casing tongue, that is discretised into several pipes. In a second stage, the fluid accelerates towards the rotor entry through a network of pipes (connecting pipes), linking the casing tongue and the rotor. Circumferential variation in volute conditions and the admittance of mass into the rotor through all blade passages is accounted for, by means of a series of small convergent ducts. The following assumptions have been made to develop the models for casing and rotor:

- the fluid is a perfect gas;
- the flow is one-dimensional and adiabatic;
- the residence time of the flow inside the turbine rotor is considered negligible, if compared to the time scale of the other phenomena involved; hence, quasi-steady effects dominate the flow in the rotor. On the basis of this assumption, a steady flow model based

on the steady maps of the turbocharger turbine can be used in a quasi-steady way to model the rotor, based on typical maps (Figure 5); this avoids the difficulty of modeling the complicated unsteady flow in the rotor. At the same time, all the unsteady effects that are mainly related to the mass storage in the turbine, have been included in the volute and in the diffuser, which are modeled by tapered pipes.

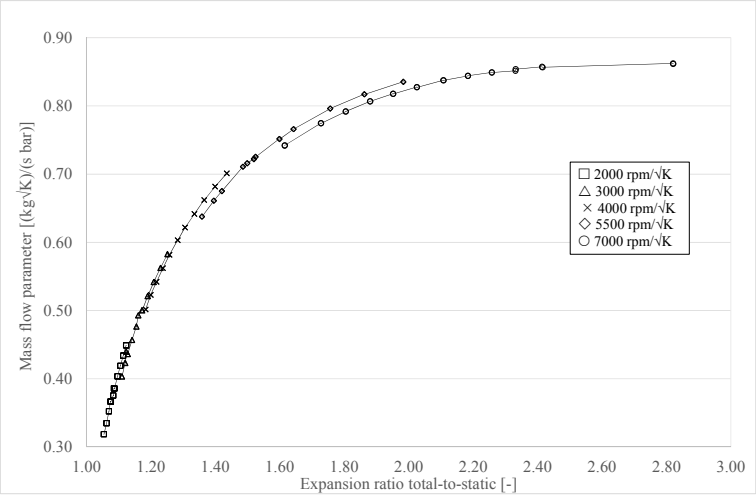

Figure 5. *Turbine steady-state characteristics measured at the turbocharger test rig of the University of Genoa.*

Since the rotor model for steady flow is a turbine model, no reverse flow from the rotor to the casing is allowed during the unsteady flow calculation. The simulation has shown that this limitation is not critical, even when instantaneous pressure ratios across the turbine are close to unity.

2.1 Variable outlet pressure quasi-steady model of the turbine rotor

Both axial-flow and radial- flow gas turbines can be used in turbochargers for automotive application. Since radial turbines exhibit a strong dependence of flow characteristics on rotational speed, their behavior looks more difficult to model. Usually, the optimum turbine speed parameter, defined as:

$$N_s = \frac{n}{\sqrt{T_{01}}} \tag{2}$$

is lower for radial flow gas turbines than for axial flow gas turbines. In general, most of the turbines used for turbocharged IC engines are designed without guide blades in the stator and with radial blades in the rotor, with a reaction degree around 0,5. In order to correctly evaluate the operating conditions of a turbocharger, the pressure downstream of the turbine cannot be assumed as a constant, if correct predictions of the instantaneous pressure ratio must be achieved. Hence, the wave equations along the inlet and outlet pipes must be coupled to the turbine flow characteristics. The boundary condition developed for the turbine rotor is an extension of that proposed by Benson [24] and solves the governing equations by means of the method of the characteristics (MOC).

In particular, the wave equations are combined with the turbine flow characteristics (see Figure 5). Indicating by the subscript "1" the turbine inlet end (point B in Figure 4), and by the subscript "2" the turbine outlet end (point C in Figure 4), the Riemann variables may be written as follows:

$$\lambda_{in,1} = A_1 \left(1 + \frac{k-1}{2} M_1\right) \tag{3}$$

$$\lambda_{out,1} = A_1 \left(1 + \frac{k-1}{2} M_1\right) \tag{4}$$

$$\lambda_{in,2} = A_1 \left(1 + \frac{k-1}{2} M_2\right) \tag{5}$$

$$\lambda_{out,2} = A_1 \left(1 + \frac{k-1}{2} M_2\right) \tag{6}$$

where M = U/A is the Mach number, U =u/ a_{ref} and A = a/a_{ref} is the non-dimensional speed of sound. The entropy change across the turbine is given by [24]:

$$\frac{a_{A2}}{a_{A1}} = \left(\frac{T_2}{T_1}\right)^{\frac{1}{2}} \left(\frac{p_1}{p_2}\right)^{\frac{k-1}{2k}} \tag{7}$$

The mass flow rate through the turbine is:

$$\dot{m} = \rho_1 u_1 F_1 = \rho_2 u_2 F_2 \tag{8}$$

where F_1 is the pipe area at the entry to the turbine and F_2 is the area connecting the turbine to the outlet pipe. By combining Eq. (7) and (8) it follows:

$$G_n = \frac{\dot{m}\sqrt{T_n}}{p_n} = M_n\sqrt{\left(\frac{k}{R}\right)}F_n \qquad \text{n=1,2} \tag{9}$$

Eq. (9) allows to find a relationship between pressure and temperature in sections l and 2:

$$G_2 = \left(\frac{p_1}{p_2}\right)\left(\frac{T_2}{T_1}\right)^{\frac{1}{2}} G_1 \tag{10}$$

Eq. (3)-(6) may be combined with Eq, (7)-(l0) and can be written as:

$$\begin{cases} \dfrac{\lambda^*_{in,1}}{\lambda^*_{in,2}} = \left(\dfrac{p_1}{p_2}\right)^{\frac{k-1}{2k}} \left(\dfrac{1+C_1G_1}{1-C_2G_1\left(\dfrac{p_1}{p_2}\right)\left(\dfrac{T_2}{T_1}\right)^{\frac{1}{2}}}\right) \\ \dfrac{\lambda^*_{out,1}}{\lambda^*_{in,1}} = \left(\dfrac{1-C_1G_1}{1+C_1G_1}\right) \\ \dfrac{\lambda^*_{out,2}}{\lambda^*_{out,1}} = \left(\dfrac{p_2}{p_1}\right)^{\frac{k-1}{2k}} \left(\dfrac{1+C_2G_1\left(\dfrac{p_1}{p_2}\right)\left(\dfrac{T_2}{T_1}\right)^{\frac{1}{2}}}{1-C_1G_1}\right) \end{cases} \tag{11}$$

where λ* is the starred Riemann variable, defined as follows:

$$\lambda^* = \frac{\lambda}{A_A} \tag{12}$$

where A_A is the entropy level. The temperature ratio T_2/T_1 across the turbine is calculated by the turbine efficiency steady characteristics. From the definition of turbine efficiency:

$$\eta_{TS} = \frac{1-\dfrac{T_2}{T_{01}}}{1-\dfrac{T_{2s}}{T_{01}}} \tag{13}$$

where T_{2S} is the outlet temperature in isentropic condition and by combining Eq. (13) with

$$\frac{T_{2s}}{T_{01}} = \left(\frac{p_2}{p_{01}} \right)^{\frac{k-1}{k}} \tag{14}$$

it follows:

$$\frac{T_2}{T_{01}} = 1 - \eta_{TS} \left\{ 1 - \left(\frac{p_2}{p_{01}} \right)^{\frac{k-1}{k}} \right\} \tag{15}$$

and

$$\frac{T_2}{T_1} = \left(\frac{T_2}{T_{01}} \frac{T_{01}}{T_1} \right) \tag{16}$$

This algorithm is applied from zero to the maximum flow rate parameter. Since the model has been devised to work mainly on engine applications, the hypothesis that no reverse flow can occur in the turbocharger turbine during the normal engine working operating conditions has been considered. In case of reverse flow, the turbine boundary condition works as a closed end, so that a pressure wave (having the same magnitude of the incident one) is reflected back from the turbine outlet towards the exhaust end. Hence, the steady flow characteristics, representing the turbine performance data, are processed from zero up to the mass flow rate corresponding to the choked flow condition. The system of the governing equations is solved iteratively, until a value M_1 that allows for the convergence of the incident, corrected Riemann variable:

$$\lambda_{in,c} = \lambda_{in,n} + \left[\frac{\lambda_{in,c} + \lambda_{out,c}}{2} \right] \tag{17}$$

is found.

In order to obtain the whole boundary curves, it is necessary to extrapolate the measured, constant speed lines back to zero mass flow. The boundary curves deriving from the

steady characteristics relate $\lambda_{in,1}$ and $\lambda_{in,2}$. The upper bound of the area is defined by the choked flow and the lower bound by no flow.

2.2 The Casing Model

Two different choices to model the turbocharger turbine have been pursued and compared in this work, following the schematic described in Figure 6.

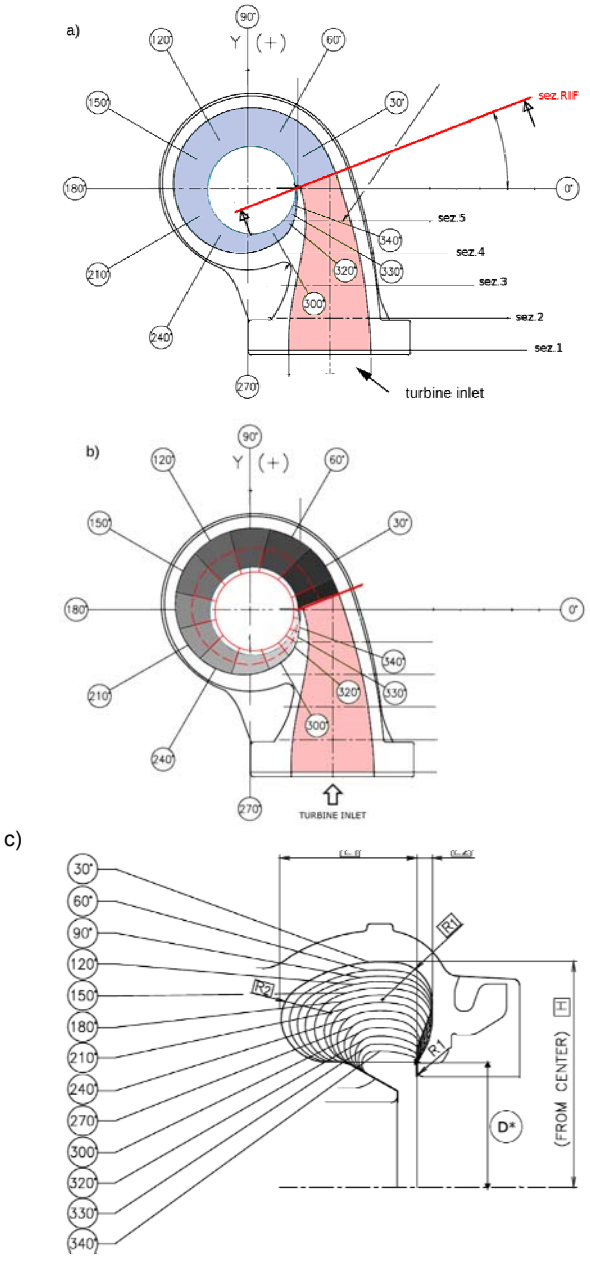

Figure 6. *Different choices to model the turbocharger turbine are compared in this work: a) the volute is represented by a tapered pipe with an open end: the entire flow is forced to pass through the rotor by the same point [14]-[17]; b) the volute is discretized into a set of elements in the streamwise direction by a network of pipes; c) variation of cross-sectional area along the volute.*

All of them use quasi-steady state maps for the rotor, but they differ from each other in the modeling of the turbine casing:

a) the tapered pipe representing the volute terminates with one open end, or rather, the entire flow is forced to pass through the rotor in one go, at the same point [14]. The pipe cross area has been set to give the correct volute volume;

b) the volute is divided into a network of pipes, so that the circumferential variation of fluid dynamic conditions along the volute and the variable admittance of mass into the rotor through all blade passages is accounted for, resorting to a series of small convergent ducts. The length of the convergent ducts is equal to the clearance between the rotor blade passages and the volute.

In both the modeling approaches outlined above, the 1D volute domain matches the corresponding length on the test facility, since validation has taken place against the mass flow characteristics (swallowing capacity) for each pulse frequency.

A one-dimensional unsteady flow analysis has been applied to the flow in the turbine volute and in the diffuser [22]; compressible conservation equations for the flow, written for the global reference frame, have been solved:

$$\begin{cases} \dfrac{\partial(\rho F)}{\partial t} + \dfrac{\partial(\rho u F)}{\partial x} = 0 \\ \dfrac{\partial(\rho u F)}{\partial t} + \dfrac{\partial(\rho u^2 F + pF)}{\partial x} = p\dfrac{\partial F}{\partial x} - \dfrac{2}{D}\rho u|u| f_w F \\ \dfrac{\partial(\rho e_0 F)}{\partial t} + \dfrac{\partial(\rho e_0 u F + upF)}{\partial x} = \rho q F \end{cases} \tag{18}$$

The system of equations in the inner nodes of the domain is solved by means of an explicit, staggered method with second order accuracy in space and time; a flux-limiting technique [18] is applied to limit spurious oscillations. In the system of equations (18), the source term for area variation is not able to give the correct contribution to account for the expansion ratio of the flow through the fluid machine and for flow behavior in the

rotor channels. For this reason, in the proposed approach the expansion ratio is still calculated through the steady-maps of the turbine, while the network of pipes is demanded to describe the effects due to the volume blockage of the flow in the machine. As it will be shown, these effects become more and more important as the unsteadiness of the flow becomes significant; the physical meaning given to the connecting pipes, describing the volute and the diffuser, influences the definition of their length and the simulation results. In other words, the simulation can be improved if the available steady flow map refers to the effective expansion ratio across the rotor and not across the whole turbomachine.

3. Model validation

A comparison between experiments and simulations for the two turbine modeling approaches has been carried out, to investigate the capability of the model to predict the effects of the unsteady flows. The rotational speed of the turbocharger shaft was set constant and equal to 4000 rpm/√K (corresponding to a turbocharger rotational speed of 75000 rpm); hence, no power balance was calculated at the shaft. This choice is consistent with the procedure followed in the experiments, where the rotational speed was kept almost constant by controlling the pressure ratio across the compressor power absorption [17]. Simulations were performed by varying the inlet flow conditions, namely the pulse amplitude (hence the mean expansion ratio $\varepsilon_{mean}=p_{in}/p_{out}$ across the system, referring to the static condition) and the pulse frequency f. According to the schematic of Figure 4, for different combinations of frequency f and ε_{mean}, the comparison between simulation results and experiments were carried out in terms of:

- instantaneous pressure at point A, B and C of Figure 4;
- instantaneous temperature upstream of the turbine, point B of Figure 4;
- instantaneous expansion ratio $\varepsilon_{mean}=p_B/p_C$, defined as the ratio between the

instantaneous pressures across the device (point B and C, Figure 4);

- instantaneous mass flow rate $\dot{m}$;

- swallowing capacity traces, relating the instantaneous quantities upstream of the turbine (through the mass flow parameter $= \frac{\dot{m}_B\sqrt{T_B}}{p_B}$) with the instantaneous expansion ratio ε. In particular, only the plots of swallowing capacity are reported for first-level turbine model, since in this case the predictions significantly deviate from the experimental traces. Conversely, comparisons on all the quantities described above are described for the second-level turbine model, in order to prove its capability to correctly capture the physics of phenomena under different operating conditions. Finally, an analysis based on dimensionless criteria to quantify levels of unsteadiness is discussed in the last section.

3.1 First-level turbine model

The first-level model is a small enhancement of the approach described in [17] and applies a basic interpretation of the experimental turbine volute: the housing of the turbine is discretised by one convergent duct, whose length is that of the housing measured along the tangential direction in the CAD file. The one-dimensional domain representing the turbine volute must match the corresponding test facility in terms of length and volume, in order to capture fluid inertia effects (filling-and-emptying). In Figure 7, plots of the instantaneous expansion ratio against the mass flow parameter are shown: the comparison is performed for different expansion ratios ε_{mean} (static to static) across the system and pulse frequencies of the pressure signal. The typical clockwise hysteresis loop, surrounding the steady state curve, between pressure ratio and mass flow parameter can be detected with some discrepancies. This aspect is due to the fact that, at the typical pulsating flow frequencies of automotive engines, the pulse is so rapid that the volume of the turbine volute is not incrementally filled with pressure. The dashed line represents the

prediction of the steady state model, commonly adopted in IC engine simulation codes: since the model is based on steady-state maps, it provides a biunivocal correspondence between the mass flow parameter and the instantaneous expansion ratio.

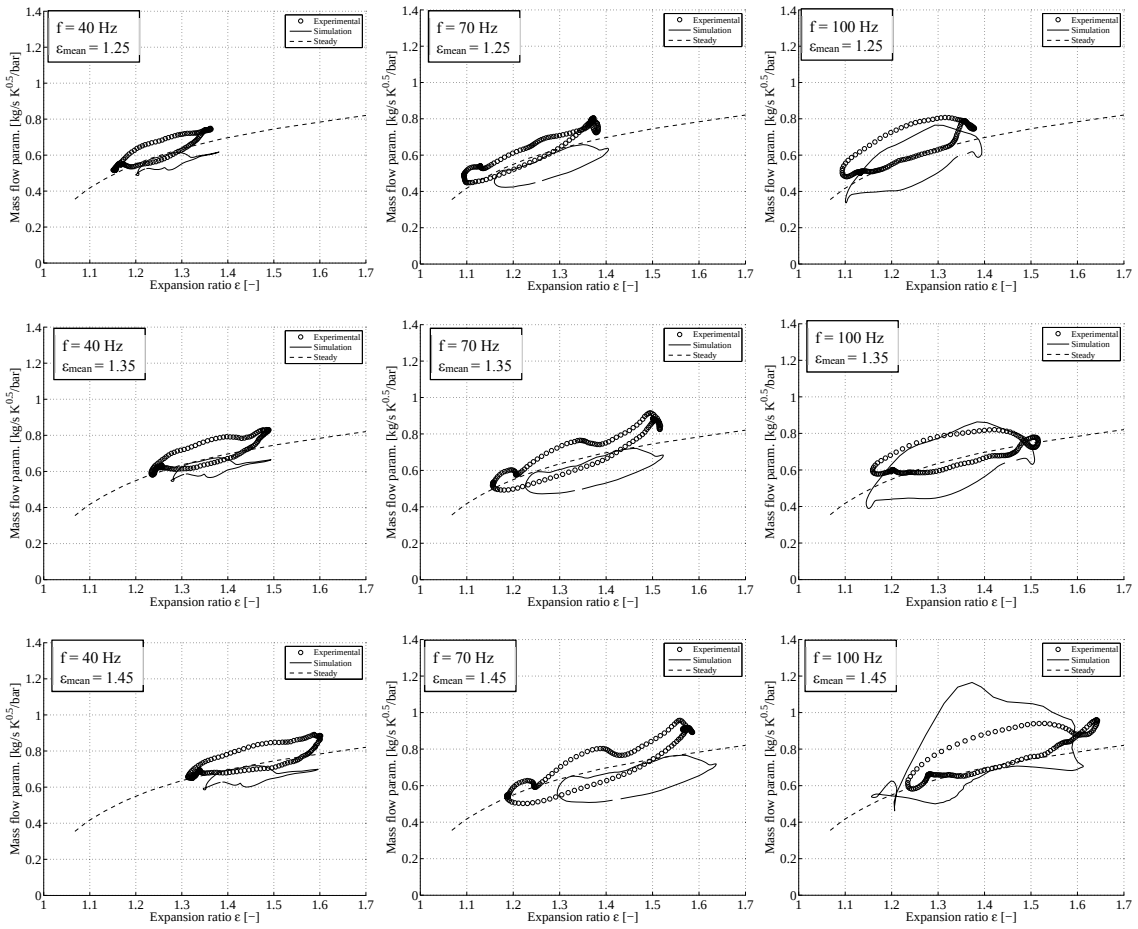

Figure 7. *First—level turbine model. Instantaneous expansion ratio against mass flow parameter. Tests are performed at different values of the mean expansion ratio ε_{mean} and pulse frequency of the pressure signal.*

However, despite the first-level approach to model the turbine ~~still~~ looks quite simple and is able to capture some features of the swallowing capacity, in general its ability to predict the unsteady mass flow characteristics is not fully satisfactory for all the frequencies tested, hence its applicability remains questionable. This is due to the way the housing of the turbine is modeled: using a unique long, convergent pipe connected to the rotor through a single connecting pipe leads to assume that the flow admission to the rotor

occurs only in one point.

3.2 Second-level turbine model

The second, more complex approach consists of dividing the curved volute pipe into a network of ducts. Circumferential variation in volute conditions and variable admittance of mass into the rotor through all blade passages is accounted for, resorting to a series of small convergent ducts, whose length is measured by the CAD along the mean diameter D_{mean} of the volute. Passages are treated as individual ducts; care must be taken here to ensure that these pipes follow the mean-line flow (see Figure 8).

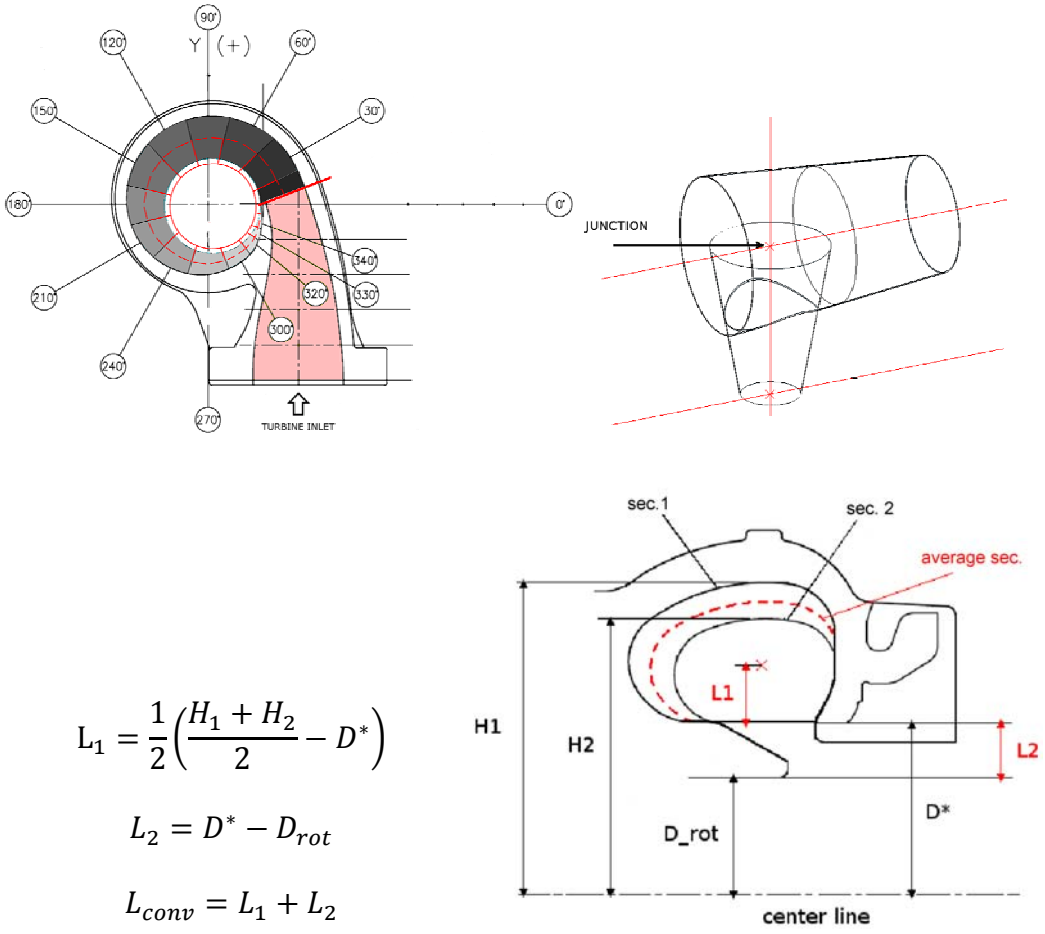

$$L_1 = \frac{1}{2}\left(\frac{H_1 + H_2}{2} - D^*\right)$$

$$L_2 = D^* - D_{rot}$$

$$L_{conv} = L_1 + L_2$$

Figure 8. *Second-level turbine modeling approach: the housing of the turbine is discretized by several convergent ducts, connected to the rotor boundary condition by a series of short convergent pipes, whose length is* L_{conv}.

Ducts representing the volute are linked to the rotor boundary condition by several short convergent pipes, that are used to model the connection between the volute and the rotor

channels (see Figure 9); the resulting discretization allows to match the original volume of the turbine volute, experimentally measured.

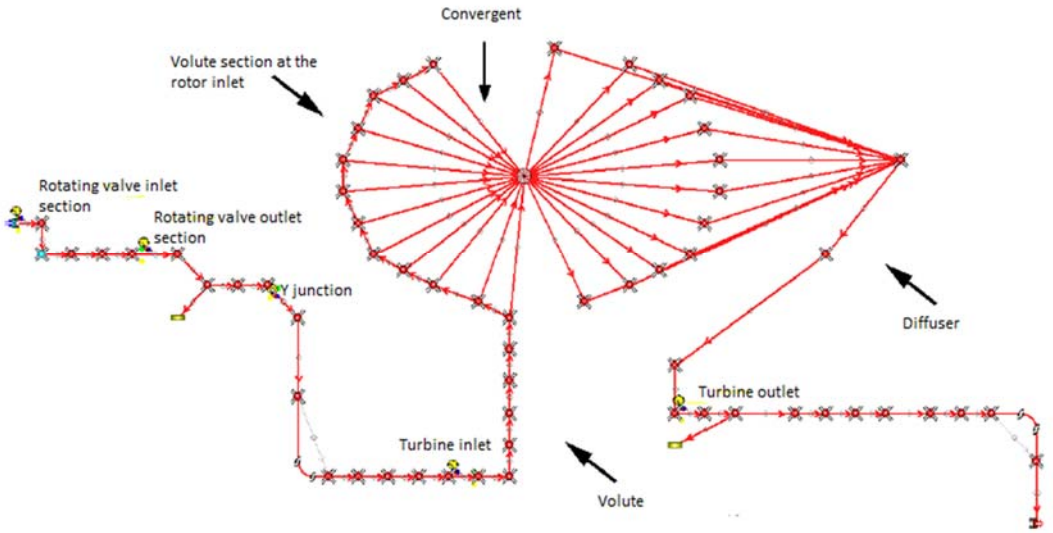

Figure 9. *One-dimensional schematic of the second-level turbine model.*

Bend losses have also been included in the modeling, to take into account the curvature of the volute. As confirmed by Figures 10 to 18, this way to model the turbine leads to a satisfactory prediction of the swallowing capacity, with a significant improvement with respect both to the first-level model described above and to the previous studies of the same authors [17].

In fact, the comparison between experiments and simulation on the plotted quantities shows an improvement with respect to the first-level turbine model for low and medium frequency and amplitudes of the signal (Figures 10 and 11). In Figure 10, the turbine instantaneous mass flow parameter is plotted against the expansion ratio and compared with steady flow performance for different operating conditions. In general, a better prediction of the hysteresis loop is achieved for 40 Hz and 70 Hz. An increase in the loop area was found at higher mean inlet pressure levels and high frequency (100 Hz), where the flow unsteadiness is more significant, maybe due to the wave action in the upstream turbine circuit. The mass flow rate oscillation amplitude also grew significantly at higher mean expansion ratio, due to the increase in the mean mass flow ~~level~~ and the relative inertial effects. Besides, at 70 and 100 Hz the steady state curve is no longer encapsulated by the unsteady curve. As reported by other Authors [11], this may be due to the fact that there is not enough time to fill the volute volume before the peak of the pulse is reached.

As highlighted in Fig. 11-16, the change in pulse frequency induced modifications of measured traces as a result of wave reflections in the upstream circuit between the pulse generator and the inlet measuring section.

It must be highlighted that experimental temperatures plotted in Figures 11-16 refer to an adiabatic process of an ideal gas (Eq. 1). At high frequency (100 Hz), the second-level turbine model seems not to behave as expected; in order to justify this unexpected behavior, a detailed investigation of the instantaneous quantities (instantaneous expansion ratio, instantaneous pressure and temperature) of the gas across the device is provided.

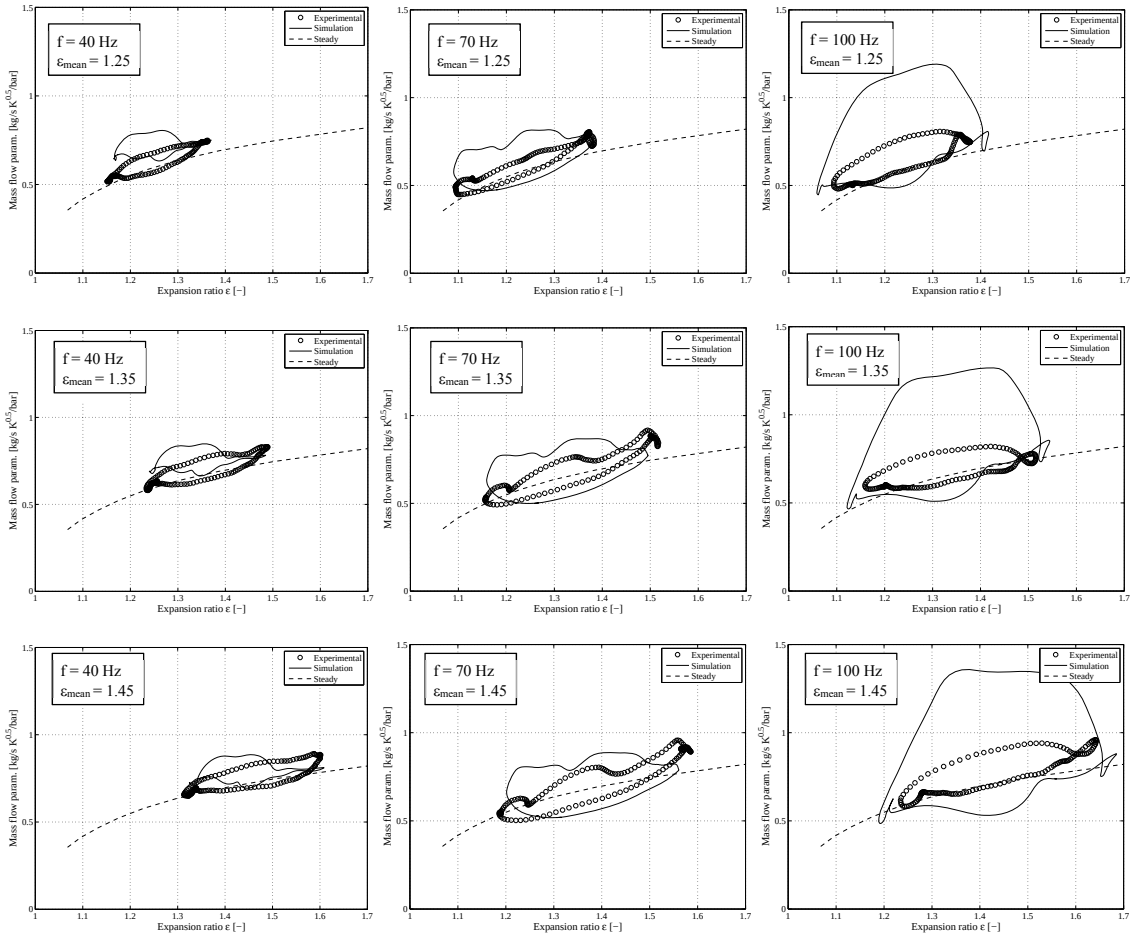

Figure 10. *Second-level turbine model. Instantaneous expansion ratio against mass flow parameter. Tests are performed at different values of the mean expansion ratio* ε_{mean} *and pulse frequency of the pressure signal.*

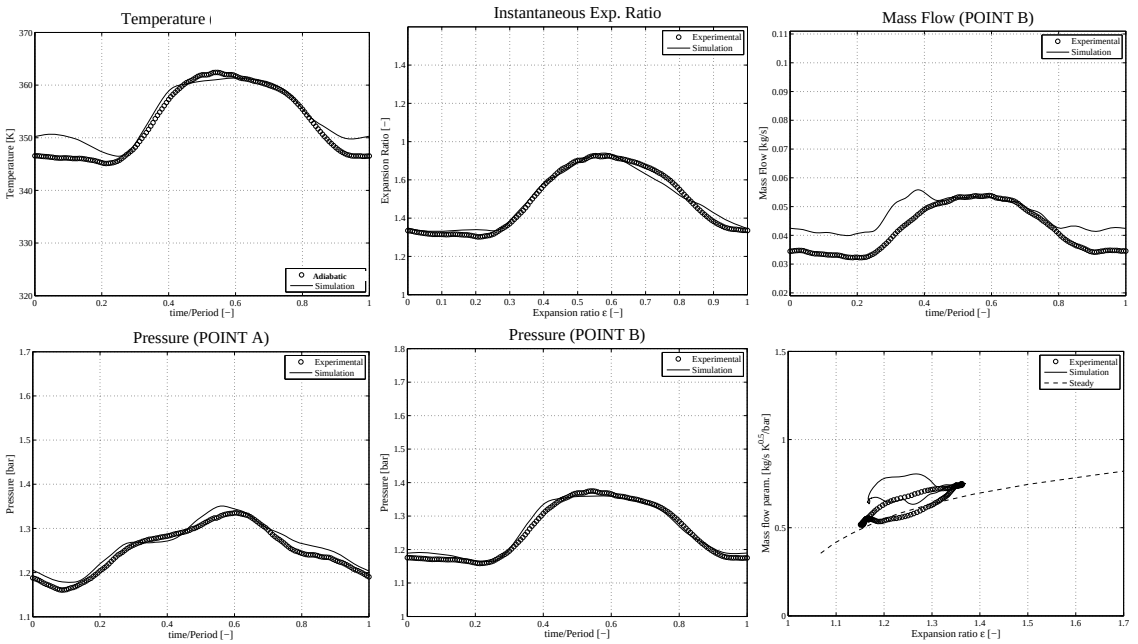

Figure 11. *Second-level modeling approach: comparison between simulations and experiments for different flow quantities. Pulse frequency of the pressure signal f= 40 Hz, mean flow expansion ratio ε_{mean} =1.25. Point A and B are referred to different locations of the system reported in Figure 4.*

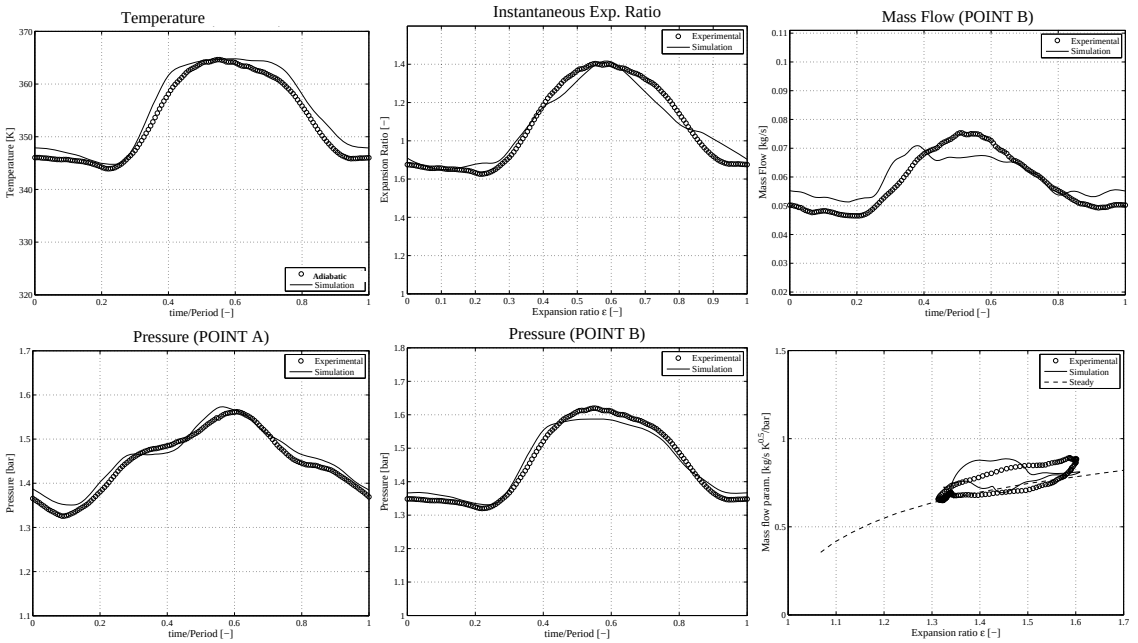

Figure 12. *Second-level modeling approach: comparison between simulations and experiments for different flow quantities. Pulse frequency of the pressure signal f= 40 Hz, mean flow expansion ratio ε_{mean} =1.45. Point A and B are referred to different locations of the system reported in Figure 4.*

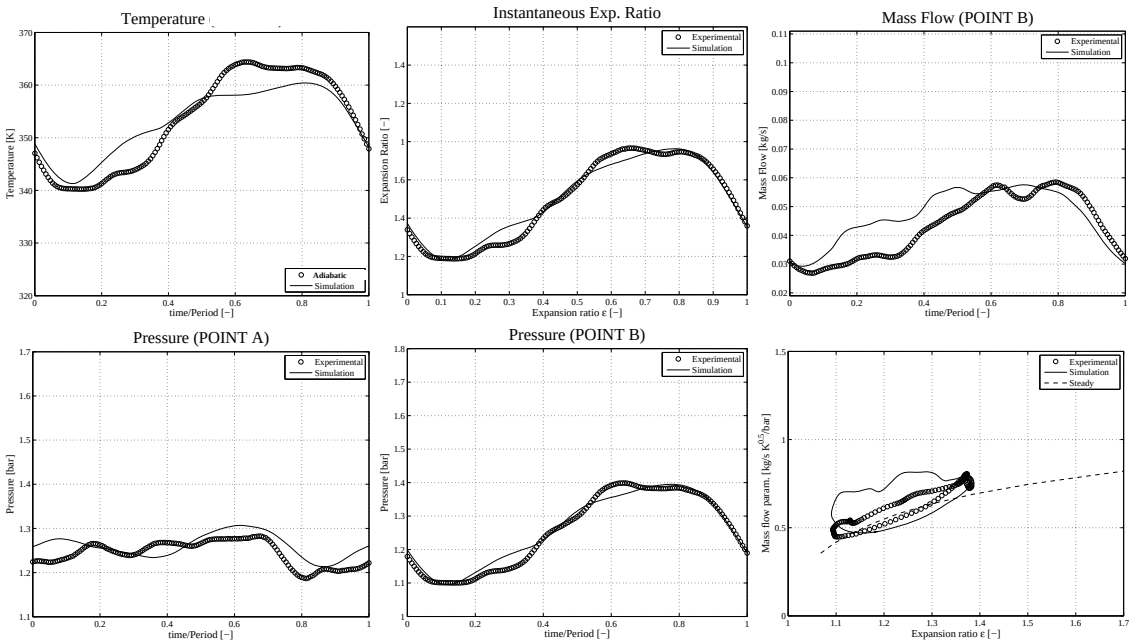

Figure 13. *Second-level modeling approach: comparison between simulations and experiments for different flow quantities. Pulse frequency of the pressure signal f= 70 Hz, mean flow expansion ratio ε_{mean} =1.25. Point A and B are referred to different locations of the system reported in Figure 4.*

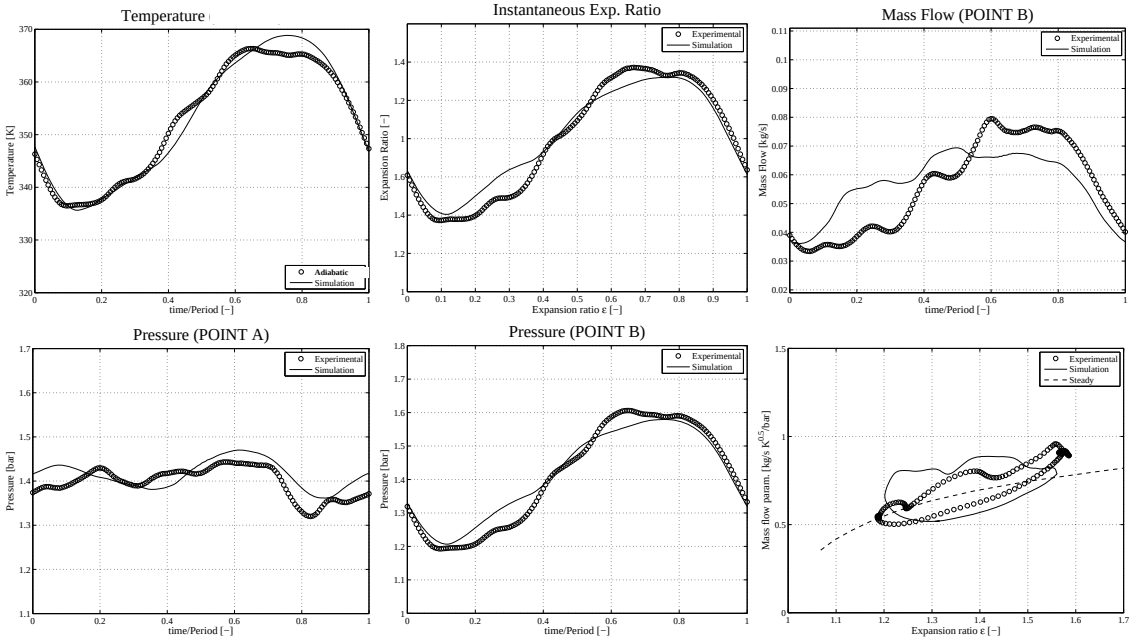

Figure 14. *Second-level modeling approach: comparison between simulations and experiments for different flow quantities. Pulse frequency of the pressure signal f= 70 Hz, mean flow expansion ratio ε_{mean} =1.45. Point A and B are referred to different locations of the system reported in Figure 4.*

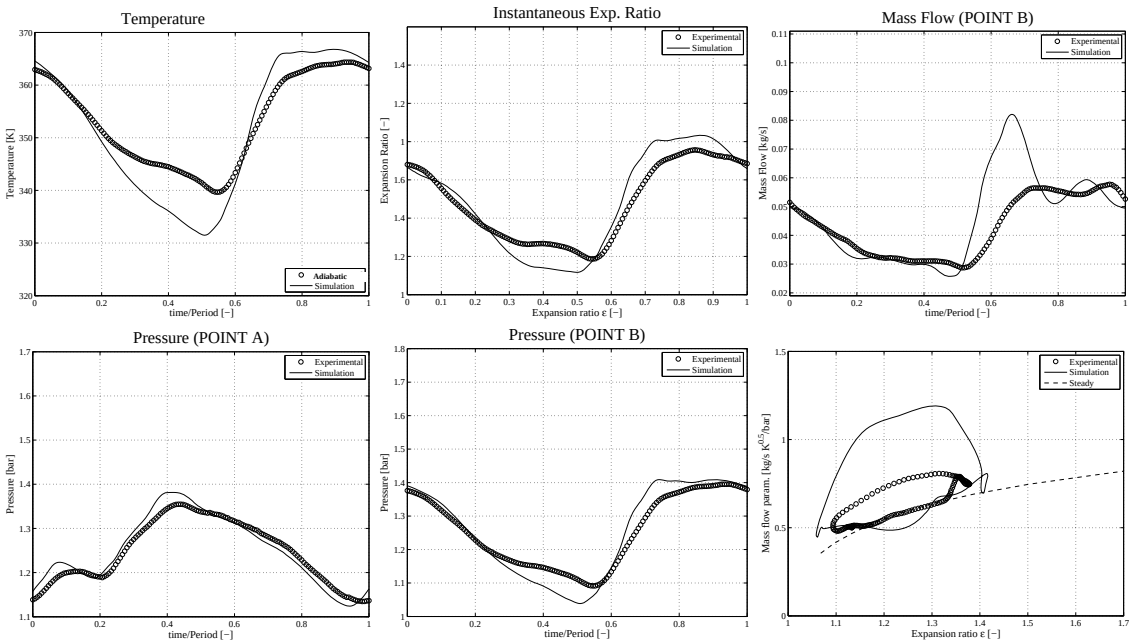

Figure 15. *Second-level modeling approach: comparison between simulations and experiments for different flow quantities. Pulse frequency of the pressure signal f= 100 Hz, mean flow expansion ratio ε_{mean} =1.25. Point A and B are referred to different locations of the system reported in Figure 4.*

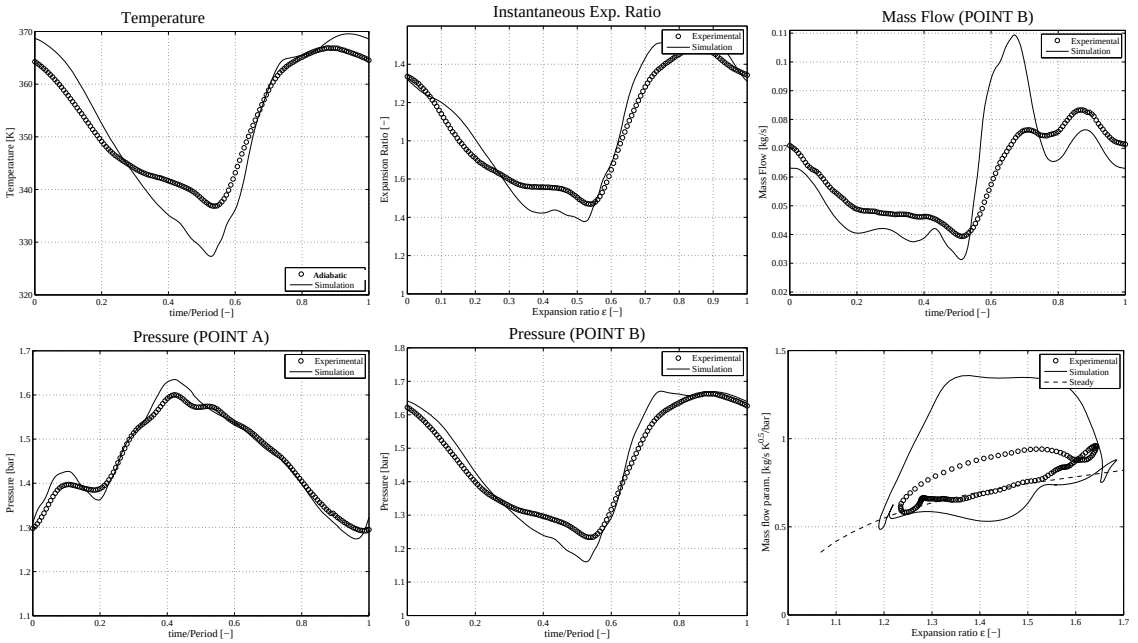

Figure 16. *Second-level modeling approach: comparison between simulations and experiments for different flow quantities. Pulse frequency of the pressure signal f= 100 Hz, mean flow expansion ratio ε_{mean} =1.45. Point A and B are referred to different locations of the system reported in Figure 4.*

The experimental temperature profile at the turbine inlet proved to be related to the measured pressure signal (Figures 11-16), due to the experimental procedure followed (Eq. 1). Temperature oscillation lies between 20° C and 30° C and significantly affects the mass flow results, when used to correct the outlet signal of the hot wire probe [21]. Experimental mass flow profiles seem to follow the main features of the pressure trace: Figures 11-16 show that the agreement between experimental and predicted instantaneous mass flow is satisfactory at low and medium frequency, while is not for high frequency signals. The discrepancy between predictions and experiments in the swallowing capacity traces at f=l00 Hz (Figures 15-16) is mainly due to a discrepancy in the estimation of the instantaneous mass flow, resulting in a damped measured oscillation amplitude from 0.5 to 1 time/pulse period, probably due to the temperature signal adopted to correct the outlet signal of the hot wire probe. The mass flow rate signal was measured through a hot wire fibre film probe, located at the center of the duct near the inlet of the turbine; calibration was performed against a laminar flow meter under steady flow condition. The discrepancies between measured and calculated profiles may be attributed to a change of the flow profile in the duct, when working under unsteady flow condition.

Moreover, it seems that the first level turbine model better captures the instantaneous mass flow rate at 100 Hz (Figure 7), despite it does not fully take into account the interaction between the volute and the rotor through the blade passages; this is basically due to the fact that, when blade passages are not modeled, the inertial effects related to the flow velocity become dominant on the wave action, resulting in a dumping effect on the mass flow rate. At the same time, there are two aspects that must be taken into account when simulation data are analyzed. First, a perfect adiabatic assumption has been made for the duct walls in the 1D modeling; despite experiments were carried out with cold flow, a small heat transfer between gas and walls can occur, so this might cause a minor error in the predictions. Also, the rotational speed of the camshaft has been considered perfectly constant, while in the real experiments it was oscillating around the mean value of 4000 rpm/√K, as shown in Figure 17. The availability of measured rotational speed profile made it possible to estimate the instantaneous fluctuating power, starting from the polar moment of inertia of the turbocharger and the angular acceleration. In Figure 18 the turbine actual power, expressed as the sum of average and fluctuating power output [21], is shown.

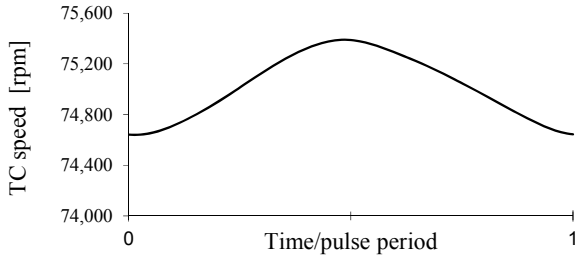

Figure 17. *The rotational speed of the turbocharger has been considered perfectly constant, while in the real experiments it was oscillating around the mean value of 4000 rpm/√K.*

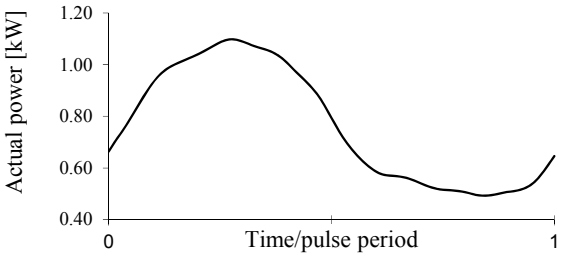

Figure 18. *Experimental actual power, evaluated at pulse frequency of 40 Hz and* ε_{mean} *=1.25 .*

4 Evaluating the unsteadiness in flow systems

In this paragraph a definition of flow unsteadiness is reported, referring to different parameters; this analysis is necessary to assess the importance of filling and emptying phenomena into the turbine volute, as well as of flow unsteadiness in the turbocharger system. The aim of this evaluation is to improve the understanding of how an unsteady flow can influence on-engine turbocharger conditions and how to reliably predict this influence, when significant. A variety of parameters can be used to quantify the effects of unsteady flow in fluid systems and, therefore, in turbocharger turbines. One such example is the dimensionless parameter known as the *Strouhal* number [25], which is used to describe oscillating flow mechanisms:

$$St = \frac{fL}{v} \tag{19}$$

In the standard application, f denotes the vortex shedding frequency (the frequency of the Karman vortex sheet generated by a cylinder in cross-flow), L is the characteristic length of the flow (e.g., a hydraulic diameter), and v is the fluid velocity (upstream of the cylinder). Although the use of the *Strouhal* number (St) is adequate for sinusoidal oscillating flows or similar, it was shown that it is important to take into account the pulse

duty cycle factor for pulses that could be identified as having distinct fluctuating (half-sinusoidal) and constant regions. The relative importance of unsteady effects produced by pulsating flows on turbocharger turbines for reciprocating engines can be estimated by the use of dimensionless criteria, as proposed by Szymko [11]:

- modified Strouhal number:

$$St^* = \frac{fL}{v} \cdot \frac{1}{2\emptyset} \tag{20}$$

the pulse correction factor Φ expresses the pulse length as a fraction of the wavelength. This is required to compensate for the non-sinusoidal nature of the experimental pulse shape, which purposely replicates that generated by an IC engine;

- reduced frequency β [26]:

$$\beta = \frac{\omega L}{v} \tag{21}$$

according to Greitzer [27], if β<<l unsteady effects are small, if β>>l unsteady effects are important, while if β=1 both unsteady and steady effects are important;

- "acoustic normalized" Strouhal number:

$$aSt = St^*(a) = \frac{fL}{a} \cdot \frac{1}{2\emptyset} \tag{22}$$

this parameter has been originally employed to measure the importance of pressure wave propagation in centrifugal compressors in [28], using a sound speed based on an average static temperature in the impeller passage;

- "pressure wave normalized" Strouhal number, where the velocity of pressure propagation is used as characteristic velocity:

$$pmSt = St^*(p) = \frac{fL}{v+a} \cdot \frac{1}{2\emptyset} \tag{23}$$

pressure wave normalized Strouhal number St(p) proved to be useful in gauging the shift to unsteady operation in cases where Φ=l [11].

In the present work, the rotational speed of the rotating valve was set to simulate the typical pulsation of a 4-cylinder engine. Assuming a four-in-one manifold and a symmetrical firing-order, the pulse correction factor Φ can be assumed equal to unity in

these cases, as suggested in [12]. In terms of a complete engine exhaust system, the most important variables regarding the dimensionless parameters *St* and β are the pipe length and the pulse frequency. Despite the length of pipes connecting the exhaust valve of each cylinder with the turbine entry slightly differs, groups of cylinders may be considered to have approximately the same duct length.

It has been found in [11] that at St*(p) ~ 0.1 the unsteady flow effects are significant; in Table 1 the parameters St*, β, aSt and pmSt have been calculated for each of the operating points simulated; results show that unsteady flow effects seem to be dependent more on the pulse frequency, rather than on the mean expansion ratio tested (i.e. on the amplitude of the pressure waves reaching the turbine inlet), that are typical of the operation of a small-displacement 4-cylinder engine. As expected, predictions at high frequency are supposed to be the most critical, as evidenced by the calculation of both the swallowing capacity at 100 Hz and the average turbine power.

Table 2 shows a comparison between the experimental turbine power and the mean turbine power (averaged over the engine thermodynamic cycle) predicted by the code:

$$\bar{W} = n_c \oint \eta_{TS}\, \dot{m} \frac{c_{is}^2}{2} dt = n_c \oint W \mathrm{d}t \qquad (24)$$

where η_{TS} is the total to static efficiency corresponding to the speed parameter $n/\sqrt{T_{01}}$ and n_c is the number of cycles per second ($n_c = 1/2$ for a 4-stroke engine).

The turbine actual power was expressed as the sum of average and fluctuating power output. The availability of measured rotational speed profile made it possible to estimate instantaneous fluctuating power, starting from the polar moment of inertia of the turbocharger rotor assembly and the angular acceleration (Figure 18). Since the turbine exhaust gas temperature measurement gives unrealistic results, due to the flow field characteristics at the radial turbine outlet, the average power was calculated on the basis of compressor power absorption, taking into account mechanical losses in the

turbocharger bearings, estimated by the heat flux to the lubricating oil flowing through the turbocharger [3].

Table 1. *Dimensionless criteria to estimate the relative importance of unsteady effects produced by pulsating flows on turbocharger turbines for reciprocating engines*

	f=40 Hz				
ε_{mean}	1.25	1.3	1.35	1.4	1.45
St*	0.3607	0.3495	0.3417	0.3326	0.3264
β	2.2661	2.1961	2.1468	2.0897	2.0507
St*(a)	0.0315	0.3150	0.0315	0.0315	0.0314
St*(p)	0.0289	0.0289	0.0288	0.0288	0.0287

	f=70 Hz				
ε_{mean}	1.25	1.3	1.35	1.4	1.45
St*	0.6344	0.6156	0.5995	0.5881	0.5881
β	3.9862	3.8681	3.7667	3.6953	3.6953
St*(a)	0.0552	0.0552	0.0552	0.0553	0.0553
St*(p)	0.0508	0.0506	0.0505	0.0506	0.0506

	f=100 Hz				
ε_{mean}	1.25	1.3	1.35	1.4	1.45
St*	0.9201	0.8845	0.8661	0.8399	0.8245
β	5.7810	5.5572	5.4421	5.2774	5.1807
St*(a)	0.0791	0.0790	0.0791	0.0789	0.0790
St*(p)	0.0728	0.0725	0.0724	0.0721	0.0721

Table 2. *Comparison between the experimental and the mean turbine power (averaged over the engine thermodynamic cycle) predicted by the code.*

	f=40 Hz			f=70 Hz				f=100 Hz	
ε_{mean}	$\bar{W}$exp [kW]	$\bar{W}$sim [kW]	Err [%]	$\bar{W}$exp [kW]	$\bar{W}$sim [kW]	Err [%]	$\bar{W}$exp [kW]	$\bar{W}$sim [kW]	Err [%]
1.25	0.764	0.786	-2.88	0.841	0.766	8.92	0.842	0.74	12.11
1.30	0.937	0.936	0.11	0.923	0.925	-0.22	0.956	0.848	11.30
1.35	1.077	1.074	0.28	1.082	1.08	0.18	1.087	0.947	12.88
1.40	1.316	1.214	7.75	1.28	1.116	12.81	1.28	1.148	10.31
1.45	1.479	1.312	11.29	1.449	1.149	20.70	1.449	1.259	13.11

As expected, the error in the prediction of the turbine power increases as the unsteady effects become more significant. In general, Table 2 shows that there is an underestimation of the power generated, especially at higher level of average expansion

ratio. This can be due to some discrepancy in the instantaneous mass flow between simulations and experiments, and to an underestimation of flow unsteadiness at high expansion ratio. In general, it is very difficult to determine the instantaneous mass flow in the experiments; a non-intrusive measurement is complex, while in simulations the reliability of the models for highly unsteady flows becomes more critical. However, the discrepancy shown in Table 2 may be considered satisfactory, considering the current state of the art of these models.

5. Conclusions

In this work a detailed approach for 1D modeling of IC engine turbochargers and an extensive experimental investigation have been presented, to study the flow conditions in a turbine under pulsating flow.

The model described is an alternative to the classical quasi-steady treatment of the turbine as a boundary condition, which assumes that the unsteady performances can be predicted by an interpolation of the steady flow mass and efficiency characteristics. This new model is able to account for the significant effect due to the volume of the turbine volute.

A one-dimensional fluid dynamic code has been enhanced to carry out the modeling of a turbocharger submitted to unsteady flows, simulating the rig developed for the experimental investigation. In particular, a rotating valve upstream has been modeled to represent the excitation source of the unsteady flows in the duct system, reaching the turbine inlet; the prediction of waves reflected at the outlet has been improved, resorting to a partially reflective boundary condition. Moreover, algorithms to extrapolate turbine performance and efficiency data maps have been implemented in the code. The compressible conservation equations for the unsteady flow have been solved by means of an explicit, staggered method with second order accuracy in space and time.

With regard to the turbine, two different 1D modeling approaches have been investigated and compared. The first, simpler one represents the volute by a tapered pipe with an open end, so that the flow passes through the rotor in one point; the pipe cross area gives the correct volute volume; a second, more detailed approach, represents the volute by a network of pipes, with variation of cross-sectional area along the volute. In this way the variation of fluid dynamic conditions along the volute and the variable admittance of mass into the rotor through all blade passages are accounted for, resorting to a series of small convergent ducts. In both methods, the expansion ratio is calculated by means of the steady-maps of the turbine, while the network of pipes accounts for the volume blockage of the flow in the machine.

In parallel, a detailed experimental analysis of the turbine has been performed at a specialized test rig of the University of Genoa, for the purpose of investigating the unsteady flow behaviour of a small automotive turbocharger turbine. For each turbine operating condition, instantaneous inlet and outlet pressure, mass flow rate and rotational speed have been measured over a large number of consecutive cycles. Turbine inlet temperature fluctuations have been related to pressure oscillations and to the measured average level through an adiabatic process. The evaluation of turbocharger instantaneous rotational speed made it possible to assess time-dependent turbine actual power under unsteady flow conditions. Analysis of the measured traces highlighted the substantial form and phase correlation between pressure, temperature and mass flow diagrams, while the rotational speed profile showed a small amplitude. The change in pulse frequency induced modifications of measured traces, as a result of wave reflections in the upstream circuit between the pulse generator and the inlet measuring section. All these phenomena greatly affected the turbine unsteady flow performance, which deviated from steady flow conditions. In particular, the instantaneous measured mass flow parameter plotted against

the turbine expansion ratio resulted in a hysteresis loop around the steady state curve, the area of which increased at higher mean pressure levels and pulse frequencies.

For the validation of the turbine model, different mean expansion ratios across the turbine were investigated, fixing the turbine rotational speed parameter to 4000 rpm/√K. Three pulse frequencies were tested (40 Hz, 70 Hz, 100 Hz), corresponding to the dominant excitation of a four-cylinder, four-stroke engine at 1200, 2000, 3500 rpm.

From the analysis of the results achieved, it is evident that the first, simpler 1D approach is able to capture some interesting features of the swallowing capacity, but the accuracy of prediction is not fully satisfactory in general. On the other hand, the second, more complex approach seems more reliable for most of the expansion ratios and pulse frequencies tested, even if some discrepancies are still evident at high frequency (100 Hz). Only a limited amount of input data (geometry of the turbine casing) and the steady-state maps of the turbine are required, which are generally available.

The accurate predicted results of the swallowing capacity could be achieved only by a detailed modeling of the geometrical features of both the diffuser and the pipe system connecting the turbine to the ambient, and by the application of a partially reflecting boundary condition, to consider the partial wave reflection at the outlet end. In fact, the development of an advanced boundary condition to model the open end led to a more accurate calculation of the instantaneous pressure downstream of the turbine and, therefore, of the swallowing capacity.

Both experiments and simulations in the present work have been performed with cold flow. Future research work will be focused on the effects of heat transfer at the walls on the predictions of turbine performance.

Appendix A. Turbine rotor modelling

There are several critical issues which need to be addressed regarding the use and extension of turbine steady flow maps to be implemented in the 1D modeling of internal combustion engines. Turbine characteristic curves are generaly summarized by a restricted series of experimental data points, which correlate the total to static expansion ratio, the mass flow parameter (defined as $\frac{\dot{m}\sqrt{T_{01}}}{p_{01}}$), the isentropic efficiency and the turbine rotational speed parameter ($\frac{n}{\sqrt{T_{01}}}$). Turbine performance and efficiency data supplied by the manufacturer are generally defined over a restricted range, not considering the effect of the waste-gate valve.

During engine operation, turbocharger turbine and compressor may operate outside of the data range; hence, a good fit of the data for extrapolation of the turbine maps for points outside of the data range is necessary. Map quality, size and aspect strongly depend on the number of experimental points supplied by the manufacturer and by the fit performed to those data. In this section, the fitting procedure adopted is described [29, 30], together with an approach to determine the quality of the data, of the fit and of the extrapolation. In particular, for a good set of data:

- optimal blade speed ratio (BSR) calculated at the maximum efficiency point for each speed line (and for each rack position, if a VGT is considered) should increase linearly with the expansion ratio PR (BSR vs PR_{fit} curve, Figure A.19a);
- operation points at maximum efficiency η increase linearly with expansion ratio PR (η curve, Figure A.19a);
- normalized mass flow $\dot{m}_{ratio}$ (indicated as MR in Figure A.19a) (defined as the ratio between the mass flow and the highest mass flow between points having maximum efficiency) versus turbine rotational speed parameter (indicated as RPM/$\sqrt{T_{01}}$ in Figure A.19b) should be linear near the origin and should be a smooth monotone positive curve with one local maximum at high speed (MR vs RPM/$\sqrt{T_{01}}$, red line in Figure A.19b).

The following notation will be adopted: a data point is an experimental point characterized by a certain mass flow, a pressure ratio and an efficiency for a given rotational speed of the turbocharger shaft; a curve is defined by a set of points having the same rotational speed and the same expansion ratio. Dimensional quantities are denoted by the subscript “act” (actual), while quantities related to the maximum efficiency point at a given rotational speed are defined as “optimum” (they are denoted by the subscript “opt").

By considering the above assumptions, fitting curves will be derived by means of theoretical considerations between the quantities involved. A least-squares linear regression (dashed line in Figure A.19a) is used to correlate the optimum BSR and PR.

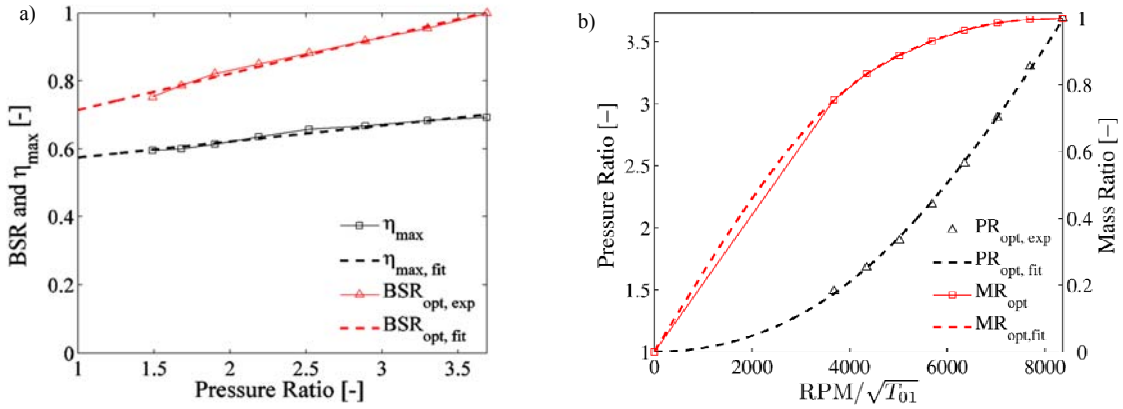

Figure A.19. *a) Optimum Blade Speed Ratio and efficiency versus Pressure Ratio; b) Pressure Ratio and Mass Ratio of optimum points versus reduced rotational speed. Hollow symbols are experimental values, dashed lines are the results of fitting.*

The Blade Speed Ratio (BSR) is defined as:

$$BSR = \frac{u}{c_{is}} \tag{A.1}$$

and the isoentropic expansion velocity c_{is}:

$$c_{is} = \sqrt{2 \cdot c_p T_{01} \left(1 - \frac{1}{PR^{\frac{(k-1)}{k}}}\right)} \tag{A.2}$$

is calculated for the same values of PR used in the fit (BSR vs. PR_{fit}). After including the

fitted values of BSR from the trace "BSR vs. PR_{fit}" into Eq. A.l, the rotor tip speed *u* can be calculated as follows:

$$u = \frac{2\pi rpm_{real}}{60}\frac{d}{2} \quad \text{(A.3)}$$

and the fitted curve "PR vs. rpm$|_{fit}$, is achieved. If the turbine diameter *d* in Eq. A.3 is unknown, an automatic procedure for its estimation is used: according to [20], at the best efficiency point of actual 90° frictionless radial turbines, the velocity ratio BSR is, generally, in the range:

$$0.68 < BSR = \frac{u}{c_{is}} < 0.7 \quad \text{(A.4)}$$

For a BSR_{opt} in that range, turbine diameter may be estimated by:

$$u = BSR_{opt} \cdot c_{is,opt} = 0.7 \cdot c_{is,opt} \quad \text{(A.5)}$$

hence:

$$d = \frac{60u}{\pi rpm_{real}} \quad \text{(A.6)}$$

where $c_{is,opt}$ is calculated by Eq. A.2. For the case of VGT turbines, to improve the diameter estimation, *d* is calculated for each rack position and for each speed line; finally, a mean value is considered. By this method, the uncertainty in the calculation of *d* looks quite high, so this procedure should be avoided when possible; on the other hand, the actual value of the diameter is not always available. When the turbine diameter is known, the blade diameter calculated from the optimum BSR may be used to detect gross errors in the input data. Maximum efficiency points are fitted and extrapolated over a wide range of expansion ratios PR. The fit has been performed by linear regression (Figure A. 19a). Also, the normalized mass flow ratio

$$\dot{m}_{norm} = \frac{\dot{m}}{\dot{m}_{opt,I}} \quad \text{(A.7)}$$

has been determined against the pressure ratio at the maximum efficiency (curve $\dot{m}_{ratio}$ vs. $PR|_{fit}$. By means of "PR vs. rpm$|_{fit}$", the MR curve vs. rpm$|_{fit}$ is built from "$\dot{m}_{norm}$ vs.

PR|$_{fit}$".

Plots of Figures A.l9a and A.l9b provide useful information about the quality of data; in particular, "PR vs. RPM/√T_{01}" represents an indicator of the overall quality of the data provided by the user. If linear regression allows for being close to "BSR vs. PR|$_{exp}$", the quality of "PR vs. rpm | $_{fit}$ " is expected to be satisfying and the fitting of the other curves reliable.

Fitting curves are used to extract values for the calculation of normalized quantities, in order to achieve non-dimensional plots for performance and efficiency maps. For each experimental expansion ratio PR_i, the optimum speed on the fitted curve "PR vs. rpm| $_{fit}$" (Figure A.l9b) is found; for a given PR, the corresponding rotational speed rpm_{opt}, at the maximum efficiency and the optimum mass flow ratio $\dot{m}_{opt}$ are known by Figure A. l9b, while the corresponding BSR_{opt} and the maximum efficiency η_{max} are achieved by Figure A.l9a. These values are used to normalize the mass flow ratio, the Blade Speed Ratio and the efficiency, as follows:

$$\dot{m}^* = \frac{\dot{m}_{exp}}{\dot{m}_{opt}} \quad \text{(A.8)}$$

$$BSR^* = \frac{\mathrm{BSR}_{exp}}{\mathrm{BSR}_{opt}} \quad \text{(A.9)}$$

$$\eta^* = \frac{\eta_{exp}}{\eta_{opt}} \quad \text{(A.10)}$$

Performance and efficiency map fit

The basic assumption in the map fitting method is, for a given turbine geometry, that all normalized experimental points may be fitted by one function, if they are plotted in the normalized mass flow rate-normalized BSR plane, as shown in Figure A.20a; similarly, all normalized efficiency points will be fitted by a single curve in the normalized BSR—normalized efficiency plane (Figure A.21a). In both cases, the fitting procedure is based

on a non-linear least-squares method. A restricted step method is used to approximate only a certain region (trust region) of the objective function; when an adequate model of the objective function is found within the trust region, the region is then expanded. Conversely, if the approximation is poor, then the region is contracted. Non-dimensional functions are shown in Figure A.20a and Figure A.21a.

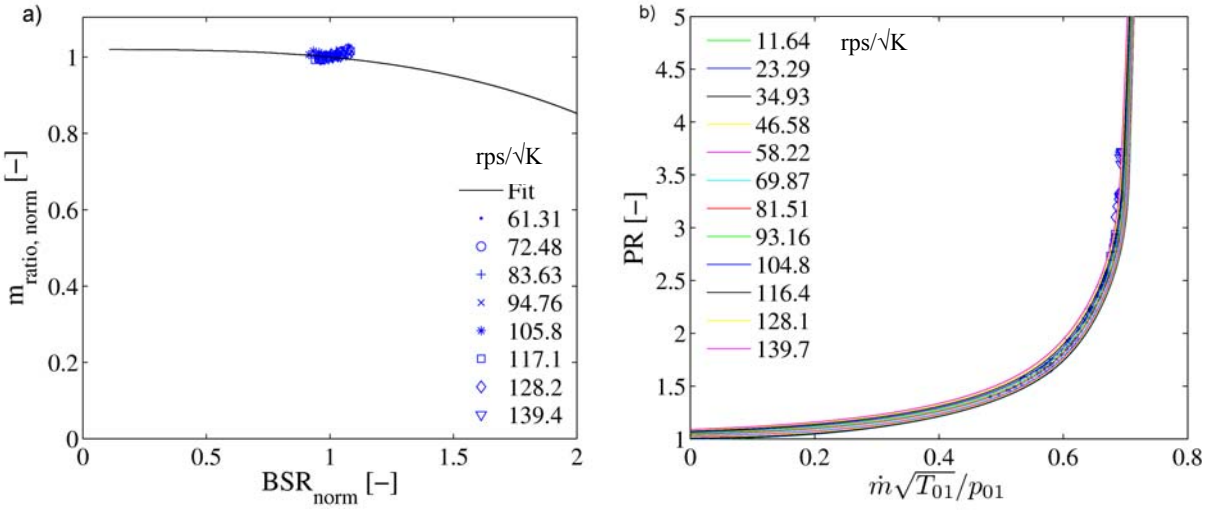

Figure A.20. *a) Normalized Mass Ratio versus Normalized BSR fitted by Eq. (A.11). Mass Ratio and BSR are normalized with their optimum value for that pressure. b) Final performance map, obtained by rescaling the smooth curve of (a).*

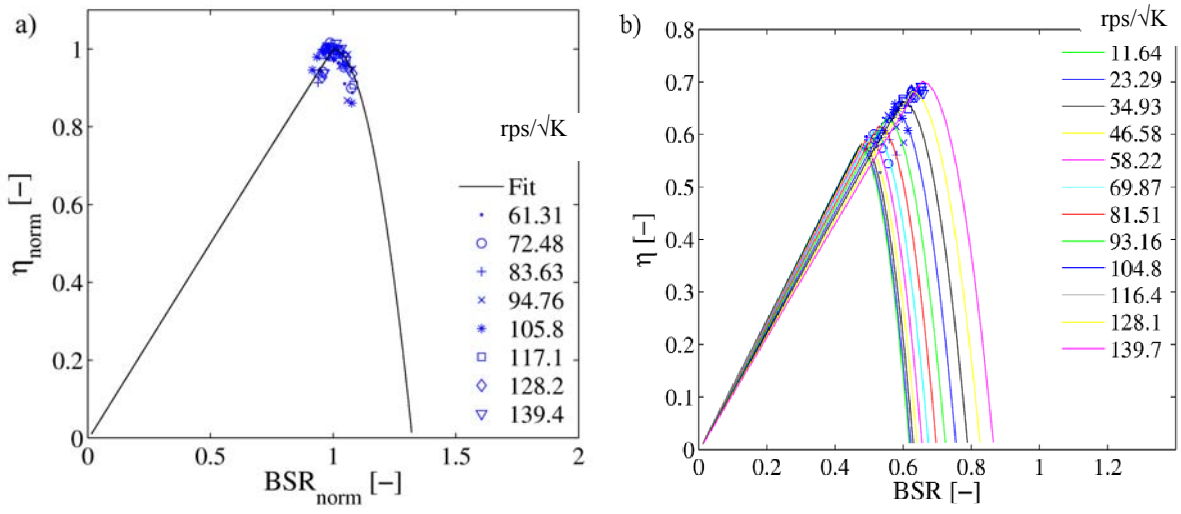

Figure A.21. *a) Fit of normalized efficiency versus normalized BSR, computed using Eq. (A.l2). b) Final efficiency map achieved by rescaling fitted curve of graph (a) for different speeds.*

The trust region algorithm performs iterations to seek the best coefficients to fit the curve in the normalized mass flow rate-normalized BSR plane by the function:

$$\dot{m}^* = a + (1-a)(BSR^*)^b \quad \text{(A.11)}$$

and the curve in the normalized BSR-normalized efficiency plane by:

$$\begin{cases} 1-(b-BSR^*)^a+(b-1)^a & \text{if } BSR^*<1 \\ 1-c(BSR-1)^2 & \text{if } BSR^*>1 \end{cases} \quad \text{(A.12)}$$

Note that each branch of the normalized fitting curve shown in Figure A.21a has a different expression, given by Eq. (A.12); the continuity of the functions for BSR=l is guaranteed by their expression.

Finally, turbine maps are built by scaling non-dimensional curves of Figure A.20a and Figure A.21a for an arbitrary range of turbocharger speeds of practical interests. For each turbocharger shaft speed, the optimum mass flow ratio *m*, the optimum Blade Speed Ratio BSR and the optimum efficiency are derived from Figure A.19a and Figure A.19b; these values will be used to rescale non-dimensional plots of Figure A.20a, in order to have the actual mass flow rates and actual BSRs for the rotational speed considered. By combining Eq. (A.l), (A.2) and (A.3), the expansion ratios PR corresponding to the actual BSRs can be found and the turbine performance map can be plotted (Figure A.20b); choked flow conditions are automatically detected by checking the slope of the characteristics. The procedure is repeated for each VGT rack position and for each rotational speed in the range considered. For the same rotational speeds, efficiency maps are calculated by scaling the non-dimensional plot of Figure A.21a, by means of BSR and efficiency η. Sometimes the manufacturer's data do not follow some expected theoretical behavior or may cover only a very small range along the speed lines. This often happens especially for data points at the lowest pressure ratios, because they are difficult to measure or because sometimes they are subsequently added to the turbine map. Due to that, those

data points do not follow the pattern of the real data and the algorithm might produce a poor fit and extrapolation of the raw data. Since data scattering looks apparent in plots having the format of Figures A.20a and A.19b, those plots are used during the fitting procedure to skip scattered data. In particular, the shape of the curve "MR vs. $rpm|_{fit}$ (red line of Figure A.19a) is strictly related to the shape of the curves in the turbine performance map; hence, it is very important that the "MR vs. $rpm|_{exp}$" diagram shows a smooth transition from the actual data to the linear line down to a null speed. In addition, its slope must be positive even at the highest flow rates, in order to correctly fit the turbine map in the choked flow region. This is automatically verified if the maximum efficiency increases linearly with the expansion ratio PR at optimum efficiency (Figure A. 19a), otherwise it must be forced. This method has proved to be sufficiently robust even if experimental data provided are not fully consistent; in this case, if a good fit is not reached, the coefficients of the interpolating curves (A.11) and (A.12) can be manually adjusted to reach a reliable trend.

Appendix B. Wave action modeling

In order to predict the unsteady behavior of the turbine, wave action modeling along the pipes has to be considered by using a partially reflecting boundary condition, to reproduce partial wave reflection at the outlet end. A detailed modeling of the geometrical features of the diffuser and of the pipe system connecting the turbine to the ambient (Figure 9) has been developed. The use of an advanced boundary condition to model the outlet end can lead to a more accurate prediction of the instantaneous pressure downstream of the turbine and, therefore, of the swallowing capacity.

Figures B.22-B.25 show the deviation in the predictions of the instantaneous pressure downstream of the turbine (point C of Figure 4) when different boundary conditions are

applied at the outlet end of the computational domain. In particular, the comparison is done between the performances of the classic constant pressure model with the PRBC model [8], where the deviation of the outlet pressure from its steady-flow value, expressed in terms of pressure rise due to the incident wave, is accounted for. The different behavior of the two models causes a discrepancy in the predictions of the instantaneous pressure trace, that becomes more apparent with high frequency pressure signals or with high amplitude pressure signals (i.e. higher ε_{mean}) and low frequency (Figures B.22-B.25). These conditions represent the range where the PRBC performs better than the constant pressure model [19]: hence, when the constant pressure model is used, the error in the estimation of the swallowing capacity is higher.

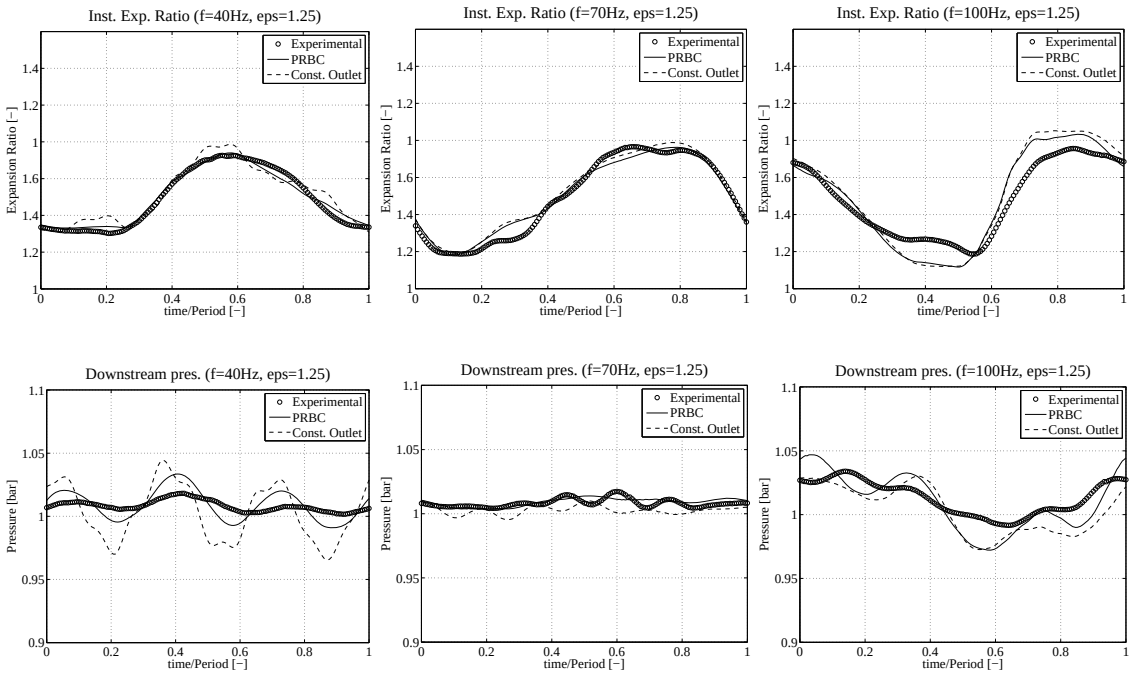

Figure B.22. *Influence of different outlet boundary conditions (PRBC vs constant pressure) in the prediction of instantaneous pressure and efficiency across the turbine. Mean flow expansion ratio across the turbine ε_{mean} =1.25. Location of Point C is reported in Figure 4.*

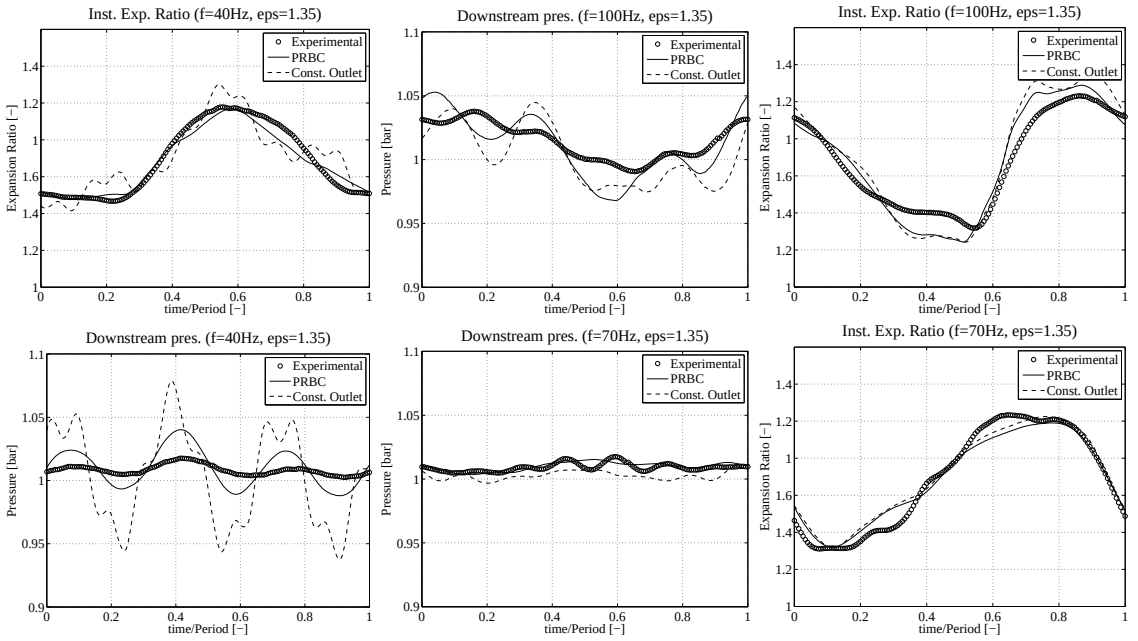

Figure B.23. *Influence of different outlet boundary conditions (PRBC vs constant pressure) in the prediction of instantaneous pressure and efficiency across the turbine. Mean flow expansion ratio across the turbine ε_{mean} =1.35. Location of Point C is reported in Figure 4.*

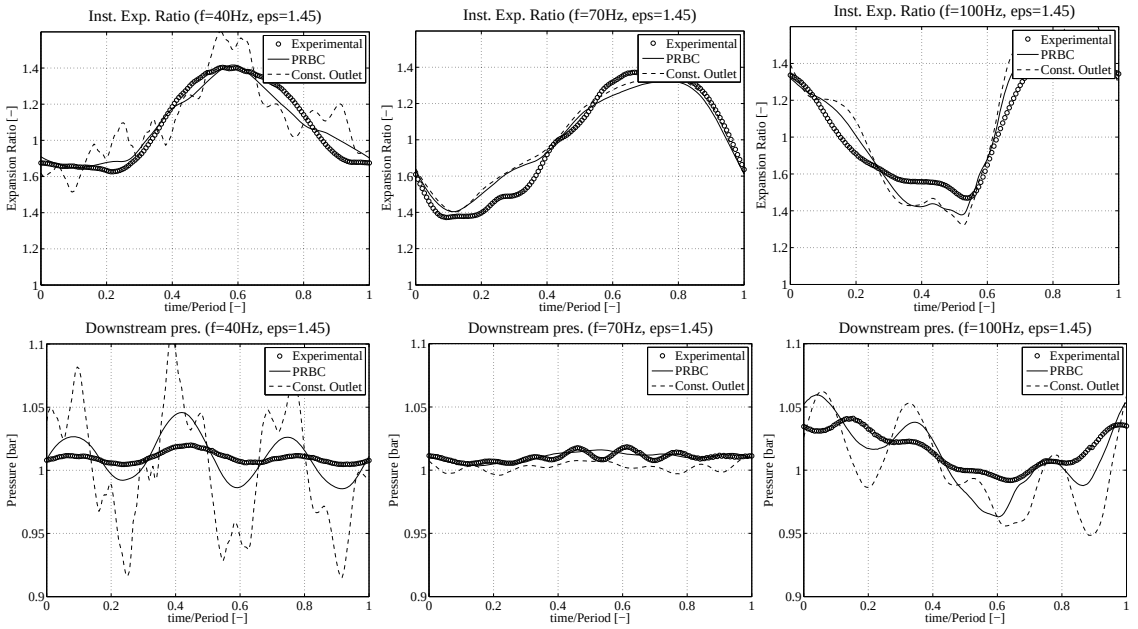

Figure B.24. *Influence of different outlet boundary conditions (PRBC vs constant pressure) in the prediction of instantaneous pressure and efficiency across the turbine. Mean flow expansion ratio across the turbine ε_{mean} =1.45. Location of Point C is reported in Figure 4.*

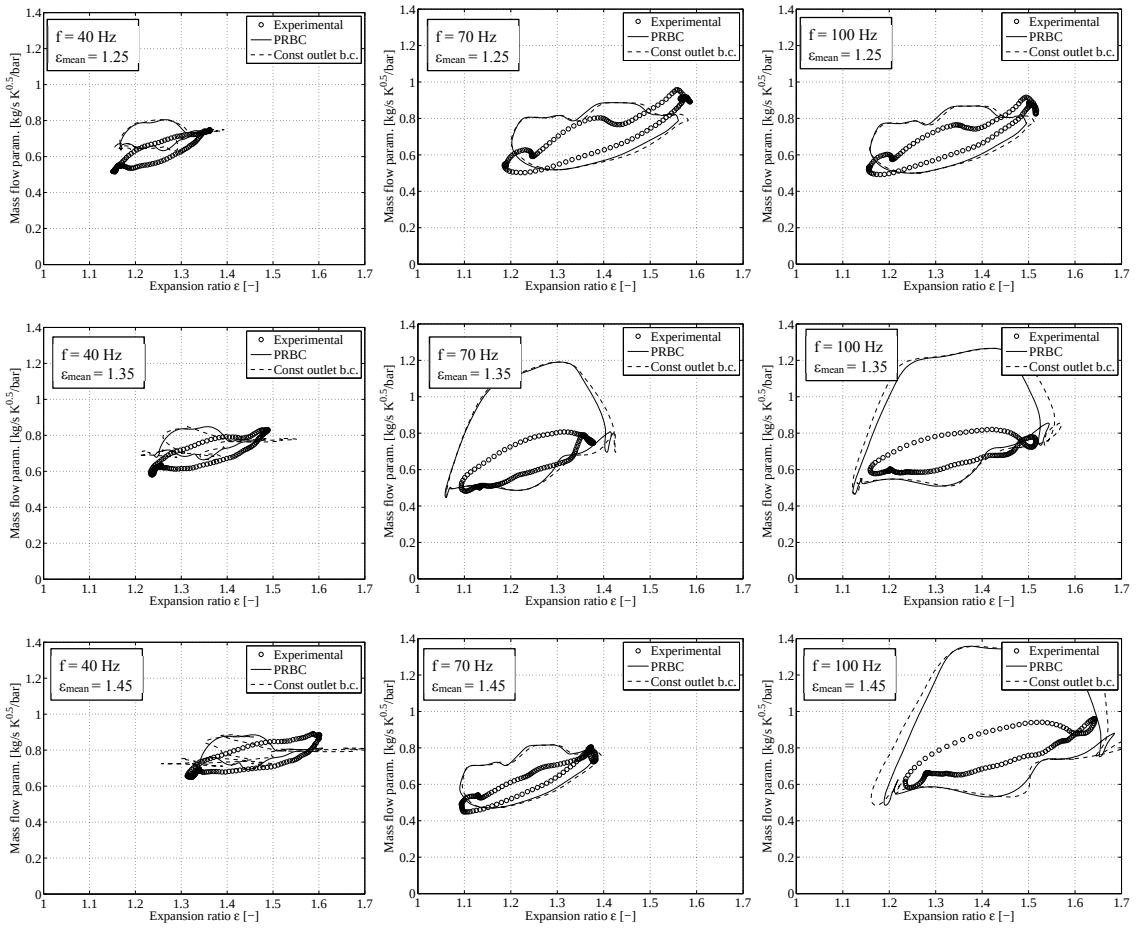

Figure B.25. *Influence of different outlet boundary conditions (PRBC vs constant pressure) in the prediction of the swallowing capacity of the turbine. As expected, the PRBC performs slightly better than the constant pressure model with high frequency signals or with pressure signals characterized by higher amplitude and low frequency.*

REFERENCE LIST

1. Bandel W, Fraidl GK, Kapus PE, Sikinger H. The Turbocharged GDI Engine: Boosted Synergies for High Fuel Economy Plus Ultra-low Emission. SAE Technical Paper 2006-01-1266.
2. Millo F, Mirzaeian M, Luisi S, Doria V, Stroppiana A. Engine displacement modularity for enhancing automotive s.i. engines efficiency at part load. *Fuel*, 2016; 180:645–652. doi:10.1016/j.fuel.2016.04.049
3. Baines N. Intake boosting, Encyclopedia of automotive engineering. John Wiley & Sons, Ltd; 2014; doi:10.1002/9781118354179.auto126.
4. Costa M, Marchitto L, Merola SS, Sorge U. Study of mixture formation and early flame development in a research GDI (gasoline direct injection) engine through numerical simulation and UV-digital imaging. *Energy*, 2014; 77: 88–96; doi:10.1016/j.energy.2014.04.114.
5. Martin G, Talon V, Higelin P, Charlet A, Caillol C. Implementing Turbomachinery Physics into Data Map-Based Turbocharger Models. SAE Technical Paper 2009-01-0310.
6. Rajoo S, Martinez-Botas RF. Unsteady Effect in a Nozzled Turbocharger Turbine.

Proceedings of ASME Turbo Expo Paper Paper No. GT2007-28323, pp. 1159-1170; doi:10.1115/GT2007-28323.
7. Macek J, Vítek O. Simulation of Pulsating Flow Unsteady Operation of a Turbocharger Radial Turbine. SAE Technical Paper 2008-01-0295, 2008, doi:10.4271/2008-01-0295
8. Galindo J, Fajardo P, Navarro R, García-Cuevas LM. Characterization of a radial turbocharger turbine in pulsating flow by means of CFD and its application to engine modeling. *Applied Energy*, 2013; 103:116–127, doi:10.1016/j.apenergy.2012.09.013.
9. Bozza F, de Bellis V, Marelli S, Capobianco M. 1D Simulation and Experimental Analysis of a Turbocharger Compressor for Automotive Engines under Unsteady Flow Conditions. *SAE International Journal of Engines*, 2011; 4: 1365-1384, doi: 10.4271/2011-01-1147.
10. Marelli S, Capobianco M, Zamboni G. Pulsating Flow Performance of a Turbocharger Compressor for Automotive Application. *International Journal of Heat and Fluid Flow*, 2014; 45: 158-165, doi: 10.1016/j.ijheatfluidflow.2013.11.001.
11. Szymko S, Martinez-Botas R, Pullen K. Experimental evaluation of turbocharger turbine performance under pulsating flow conditions. Proceedings of ASME Turbo Expo Paper No. GT2005-68878, pp. 1447-1457; doi:10.1115/GT2005-68878.
12. Serrano JR, Arnau FJ, Novella R, Reyes-Belmonte M.A. A procedure to achieve 1d predictive modeling of turbochargers under hot and pulsating flow conditions at the turbine inlet. SAE Technical Paper 2014-01-1080, 2014, doi: 10.4271/2014-01-1080.
13. Ehrlich PDA. On-engine turbocharger turbine inlet flow characterization. SAE Technical Paper 971565, SAE 48th Earthmoving Industry Conference & Exposition.
14. Chen H, Winterbone DE. A method to predict performance of vaneless radial turbines under steady and unsteady flow conditions. Turbocharging and Turbochargers, IMechI C405/008.
15. Chiong MS, Rajoo S, Romagnoli A, Costall AW, Martinez-Botas RF. One-dimensional pulse-flow modeling of a twin-scroll turbine. *Energy*, Elsevier, 2016, 115:1291-1304,doi:10.1016/j.energy.2016.09.041.
16. Serrano JR, Arnau FJ, García-Cuevas LM, Dombrovsky A, Tartoussi H. Development and validation of a radial turbine efficiency and mass flow model at design and off-design conditions. *Energy Conversion and Management*, Elsevier, 2016, 128: 281-293, doi:10.1016/j.enconman.2016.09.032.
17. Piscaglia F, Onorati A, Marelli S, Capobianco M. Unsteady behavior in turbocharger turbines: experimental analysis and numerical simulation. SAE Technical Paper 2007-24-0081, doi: 10.4271/2007-24-0081.
18. Stockar S, Canova M, Guezennec Y, Della Torre A, Montenegro G, Onorati A. Modeling wave action effects in internal combustion engine air path systems: Comparison of numerical and system dynamics approaches. *International Journal of Engine Research*, Volume 14, Issue 4, August 2013.
19. Piscaglia F, Montorfano A, Onorati A, Ferrari G. Modeling of pressure Wave reflection from open-ends in i.c.e. duct systems. SAE Technical Paper 2010-01-1051, doi:10.4271/2010-01-1051
20. Marelli S, Marmorato G, Capobianco M. Evaluation of heat transfer effects in small turbochargers by theoretical model and its experimental validation. *Energy*, Elsevier, 2016, doi:10.1016/j.energy.2016.06.067.

21. Capobianco M, Marelli S. Experimental analysis of unsteady flow performance in an automotive turbocharger turbine fitted with a waste-gate valve, *Proceedings of the Institution of Mechanical Engineers, Part D, Journal of Automobile Engineering*, 2011; 225:1087-1097.
22. Cornolti L, Onorati A, Cerri T, Montenegro G, Piscaglia F. 1D simulation of a turbocharged diesel engine with comparison of short and long EGR route solutions. *Applied Energy* , 2013, 111:1-15.
23. Winterbone D, Pearson R.J. Theory of engine manifold design, Professional Engineering Publishing, London, 2000.
24. Benson R.S. The thermodynamics and gas dynamics of internal combustion engines, Clarendon Press, 1986.
25. Douglas JF, Gasiorek JM, Swaffield JA, Jack LB. Fluid Mechanics Pearson Education Limited, Harlow, Essex, UK, 2005.
26. Landau LD, Lifshitz EM. Fluid Mechanics, Pergamon Press, 1993.
27. Greitzer EM, Tan CS, Graf MB. Internal Flow: Concepts and Applications, Cambridge University Press, 2004.
28. Fatsis A, Pierret S, Van den Braembussche RA. 3d unsteady flow and forces in centrifugal impellers with circumferential distortion of the outlet static pressure, Transactions of the ASME, Journal of Turbomachinery (1997).
29. Dixon SL. Fluid Mechanics and Thermodynamics of Turbomachinery, Elsevier Butterworth-Heinemann, 1998.
30. GT Power manuals.